First-principles investigation of microscopic mechanisms underlying hole mobilities in diamond, silicon, and germanium

Qiao-Lin Yang,[1,2] Fan-Chen Meng,[3] Wu Li,[4] Zhi Wang,[2,5] Hui-Xiong Deng,[2,5] Su-Huai Wei [ORCID],[4]
Fan-long Ning [ORCID],[1,6,7,*] and Jun-Wei Luo [2,5,†]

[1]*School of Physics and Zhejiang Key Laboratory of Micro-Nano Quantum Chips and Quantum Control,*
Zhejiang University, Hangzhou 310027, China

[2]*State Key Laboratory of Superlattices and Microstructures, Institute of Semiconductors, Chinese Academy of Sciences,*
Beijing 100083, China

[3]*Research Computing and Data, Clemson University, Clemson, South Carolina 29634, USA*

[4]*Eastern Institute for Advanced Study, Eastern Institute of Technology, 315200 Ningbo, China*

[5]*Center of Materials Science and Optoelectronics Engineering, University of Chinese Academy of Sciences, Beijing 100049, China*

[6]*State Key Laboratory of Silicon and Advanced Semiconductor Materials, Zhejiang University, Hangzhou 310027, China*

[7]*Collaborative Innovation Center of Advanced Microstructures, Nanjing University, Nanjing 210093, China*

Silicon (Si) dominates the semiconductor industry but currently suffers from significant hole mobility degradation in advanced transistors due to its abnormally low hole mobility (505 cm^2/Vs), compared to its group IV neighbors, diamond and germanium (Ge) (both $\sim$2000 cm^2/Vs). While Ge's high mobility is understandable by its lighter effective hole mass due to its narrower direct bandgap at Γ point, diamond's superior hole mobility remains difficult to understand since its bandgap is ultrawide. Conventional wisdom attributes diamond's high mobility to reduced phonon scattering due to high acoustic phonon group velocity and optical phonon frequency, overcoming its heaviest effective mass. However, our study reveals that this mechanism alone is insufficient to explain the observed mobility. We demonstrate that the diamond's abnormally light effective hole mass is a primary factor contributing to its high mobility; otherwise, its hole mobility would be approximately nine times lower than Si's. The unexpectedly light mass in diamond stems from larger transition matrix elements, resulting from substantial electronic wave-function overlap between valence and conduction bands, remarkably overcoming the effect of diamond's large bandgap. Furthermore, our investigation uncovers a unique feature in diamond's valence band structure: an inherent strain-enhanced mobility characteristic, where the top valence band manifests as a light-hole (lh) state along certain crystallographic directions (e.g., [100]), instead of the typical heavy-hole (hh) state. Contrary to prevailing assumptions, we observe a strong coupling between holes and transverse acoustic (TA) phonons, and even TA scattering dominates over longitudinal acoustic (LA) scattering in both diamond and Si, challenging the long-held belief that TA scattering is negligible. Our calculations yield a dilation deformation potential of 3.45 eV for diamond, significantly diverging from previously reported values, e.g., 7 or -35 eV. This discrepancy further highlights limitations in understanding individual scattering mechanisms in diamond using classical phenomenological models. These findings shed new light on the hole mobility in semiconductors and provide new clues to enhance further the hole mobility in group IV semiconductors towards advanced semiconductor technology nodes.

I. INTRODUCTION

Carrier mobility is a fundamental property of semiconductor materials, governing crucial device characteristics such as operation speed, circuit frequency, and sensitivity in magnetic sensors [1–6]. Enhancing carrier mobility is a critical strategy for developing faster or more energy-efficient microchips, as it can improve the transistor drive current, thereby enhancing device performance or reduce power consumption in a maintained performance level [7]. Silicon (Si) has been the cornerstone of the semiconductor industry for over half a century [8–12]. However, a significant limitation of Si is its relatively low hole mobility ($\mu_h = 505$ cm^2/Vs) compared to its electron mobility ($\mu_e = 1450$ cm^2/Vs). This disparity results in p-type transistors (PMOS) operating at only about one-third the performance of n-type transistors (NMOS) [13]. Consequently, it has stimulated tremendous efforts in past decades to seek materials with higher hole mobility to replace Si and substantially improve PMOS device performance [7]. Intriguingly, Si exhibits abnormally low hole mobility compared to its two Group IV neighbors, diamond and germanium (Ge), both of which have superior hole mobility ($\mu_h \approx 2000$ cm^2/Vs) [14,15], approximately four times that of Si. This anomalous trend has sparked extensive research

*Contact author: ningfl@zju.edu.cn
†Contact author: jwluo@semi.ac.cn

aimed at understanding and potentially overcoming the limitations of hole mobility in Si, thereby improving PMOS performance and overall microchip efficiency [7].

Despite significant advancements in first-principle calculations of carrier mobilities and extensive investigations into the transport properties of semiconductors [16–24], the underlying mechanisms responsible for the abnormal trend in hole mobility among these three group IV materials remain elusive. Previous studies have attributed the higher hole mobility of Ge to its lighter effective hole mass compared to Si [25], while the superior hole mobility in diamond has been ascribed to its large group velocity of acoustic phonons and high optical phonon frequency, which result in fewer phonons participating in carrier scattering by overcoming its heaviest effective hole mass to have a much longer hole relaxation lifetime [26–28]. However, reported effective masses in diamond vary widely, ranging from 0.4 to 2.3 m_0 [15,29–33]. Such a broad range of effective mass should correspond to a significant variation in hole mobility, making it difficult to understand why the ultrawide bandgap diamond should have an effective hole mass comparable to Si, given that its fundamental bandgap is 5.5 eV being about five times larger than that (1.12 eV) in Si and its direct bandgap is 7.3 eV being two times larger than that (3.4 eV) in Si. Furthermore, the role of interband scattering in hole mobility remains contentious. Some studies argue that intraband and interband scattering rates are comparable in magnitude [30,34–38]. Chu *et al.* [39] and Mohta *et al.* [40] have stressed the importance of the interband scattering in explaining strain-enhanced hole mobility in PMOS. Conversely, Akimoto *et al.* [28] emphasized an absence of interband scattering in diamond. Moreover, our recent work [41] has revealed a significant underestimation of the hole scattering by transverse acoustic (TA) phonons regarding the classical phenomenological models. These clues underscore the need to revisit the microscopic mechanisms underlying the anomalous trend in the hole mobility in group IV materials.

The present work addresses the abnormal hole mobility trend observed in diamond, Si, and Ge employing the *ab initio* Boltzmann transport formalism. Section II reviews the formalism of phonon-limited scattering rates and hole mobilities, establishing the theoretical framework for our investigation. In Sec. III A, we present a comparison between our first-principles calculations of hole mobilities and experimental data. The contribution of lh to the total hole mobility is examined in Sec. III B, shedding light on their role in mobility enhancement through strain engineering. Section III C offers a detailed discussion on the limiting factors affecting hh scattering and mobility. This analysis is structured around four key aspects: (1) The significance of hole-transverse-acoustic-phonon scattering matrix elements (Sec. III C 1). (2) The strong hole-optical-phonon scattering matrix elements in diamond (Sec. III C 2). (3) The important rules of the effective mass (Sec. III C 3). (4) The role of interband scattering processes (Sec. III C 4). By systematically examining these factors, we aim to provide a comprehensive explanation for the observed hole mobility trends in diamond, Si, and Ge, while offering new insights into the fundamental mechanisms governing hole transport in these semiconductors. Finally, Sec. IV summarizes our key findings.

II. METHOD

The total hole mobility at a certain temperature can be obtained as a sum of the partial band mobility μ_n weighted by occupation number p_n, as illustrated in Eq. (4) in Ref. [21]

$$
\mu_{\text{tot}} = \frac{\sum_n \mu_n \cdot p_n}{\sum_n p_n}
$$
$$
= \sum_n \mu_n \cdot o_n, \left(n = \text{hh, lh, sh}; o_n = \frac{p_n}{\sum_n p_n} \right). \quad (1)
$$

Here, o_n describes the relative concentrations of n-band holes involved in transport in relation to the total hole concentration $\sum_n p_n$, and μ_n presents the intrinsic partial band mobility for nth band. In the context of weak electric fields **E**, we can limit our analysis to the linear response of the current density, which defines the partial band mobility tensor $\mu_{n,\alpha\beta}$ (α and β run over the three Cartesian directions x, y, and z) for the nth valence band,

$$
\mu_{n,\alpha\beta} = -\frac{\int d\mathbf{k} \cdot v_{n\mathbf{k},\alpha} \partial_{E_\beta} f_{n\mathbf{k}}}{p_n}. \quad (2)
$$

Here, $p_n = \int d\mathbf{k} \cdot (1 - f_{n\mathbf{k}}^0)$ is the partial density of holes arising from the nth valence band, where $f_{n\mathbf{k}}^0$ is the equilibrium Fermi-Dirac distribution function. The group velocity is defined as $v_{n\mathbf{k},\alpha} = \hbar^{-1} \partial \varepsilon_{n\mathbf{k}} / \partial k_\alpha$ with $\varepsilon_{n\mathbf{k}}$ the eigenvalue of the state $|n\mathbf{k}\rangle$, and ∂_{E_β} is short for $\partial / \partial_{E_\beta}$. The linear response coefficients $\partial_{E_\beta} f_{n\mathbf{k}}$ can be derived by taking derivatives on both sides with respect to the electric field:

$$
(-e)E \cdot \frac{1}{\hbar} \frac{\partial f_{n\mathbf{k}}}{\partial \mathbf{k}} = \Gamma_{n\mathbf{k}}^{co}, \quad (3)
$$

where the collision rate $\Gamma_{n\mathbf{k}}^{co}$ can be approximated as [42]

$$
\Gamma_{n\mathbf{k}}^{co} = \frac{2\pi}{\hbar} \sum_{m\nu} \int \frac{d\mathbf{q}}{\Omega_{BZ}} |g_{mn\nu}(\mathbf{k}, \mathbf{q})|^2
$$
$$
\times \left\{ f_{n\mathbf{k}}(1 - f_{m\mathbf{k}+\mathbf{q}})\delta\left(\Delta\varepsilon_{\mathbf{k},\mathbf{q}}^{nm} + \hbar\omega_{\nu\mathbf{q}}\right)n_{\nu\mathbf{q}} \right.
$$
$$
+ f_{n\mathbf{k}}(1 - f_{m\mathbf{k}+\mathbf{q}})\delta\left(\Delta\varepsilon_{\mathbf{k},\mathbf{q}}^{nm} - \hbar\omega_{\nu\mathbf{q}}\right)(1 + n_{\nu\mathbf{q}})
$$
$$
- (1 - f_{n\mathbf{k}})f_{m\mathbf{k}+\mathbf{q}}\delta\left(-\Delta\varepsilon_{\mathbf{k},\mathbf{q}}^{nm} + \hbar\omega_{\nu\mathbf{q}}\right)n_{\nu\mathbf{q}}
$$
$$
\left. - (1 - f_{n\mathbf{k}})f_{m\mathbf{k}+\mathbf{q}}\delta\left(-\Delta\varepsilon_{\mathbf{k},\mathbf{q}}^{nm} - \hbar\omega_{\nu\mathbf{q}}\right)(1 + n_{\nu\mathbf{q}})\right\}, \quad (4)
$$

where $\Delta\varepsilon_{\mathbf{k},\mathbf{q}}^{nm} = \varepsilon_{n\mathbf{k}} - \varepsilon_{m\mathbf{k}+\mathbf{q}}$. Equation (4) represents the difference between the rate for an electron in the state $|n, \mathbf{k}\rangle$ to scatter out of the state (first two terms) and the rate for an electron to scatter into the state $|n, \mathbf{k}\rangle$ (last two terms). Both scattering processes can occur via phonon absorption (first and third term) or phonon emission (second and fourth term). $|g_{mn\nu}(\mathbf{k}, \mathbf{k} + \mathbf{q})|$ are the electron-phonon (e-ph) scattering matrix element, demonstrating that an electron located at the initial electronic state $|n, \mathbf{k}\rangle$ is scattered by a phonon $|\nu, \mathbf{q}\rangle$ (with branch index ν, wave vector $\mathbf{q}$ and frequency $\omega_{\nu\mathbf{q}}$) into the final state $|m, \mathbf{k} + \mathbf{q}\rangle$. $n_{\nu\mathbf{q}}$ is the occupation number of the phonon $|\nu, \mathbf{q}\rangle$ according to the Bose-Einstein distribution function. Ω_{BZ} corresponds to the volume of the first Brillouin zone (BZ). The sharp δ function is usually broadened by utilizing a broadening parameter η through a Lorentzian function. Subsequently, by employing the 'self-energy relaxation time approximation' (SERTA), we can obtain $\partial_{E_\beta} f_{n\mathbf{k}} =$

$e \frac{\partial f_{n\mathbf{k}}^0}{\partial \varepsilon_{n\mathbf{k}}} v_{n\mathbf{k},\beta} \tau_{n\mathbf{k}}^0$, where the relaxation time $\tau_{n\mathbf{k}}^0$ is associated with the imaginary part of the Fan-Migdal electron self-energy $\Sigma_{n\mathbf{k}}^{\mathrm{FM}}$ [21],

$$\frac{1}{\tau_{n\mathbf{k}}^0} = 2\mathrm{Im}\,\Sigma_{n\mathbf{k}}^{\mathrm{FM}} = \sum_{m,\nu} \frac{1}{\tau_{nm,\mathbf{k}}^\nu}$$

$$= \frac{2\pi}{\hbar} \sum_{m\nu} \int \frac{d\mathbf{q}}{\Omega_{BZ}} |g_{mn\nu}(\mathbf{k},\mathbf{k}+\mathbf{q})|^2$$

$$\times \big[(1 - f_{m,\mathbf{k}+\mathbf{q}}^0 + n_{\nu,\mathbf{q}})\delta(\varepsilon_{n,\mathbf{k}} - \varepsilon_{m,\mathbf{k}+\mathbf{q}} - \hbar\omega_{\nu,\mathbf{q}})$$

$$+ (f_{m,\mathbf{k}+\mathbf{q}}^0 + n_{\nu,\mathbf{q}})\delta(\varepsilon_{n,\mathbf{k}} - \varepsilon_{m,\mathbf{k}+\mathbf{q}} + \hbar\omega_{\nu,\mathbf{q}}) \big]. \quad (5)$$

Specifically, we carry out first-principles calculations employing QUANTUM ESPRESSO package [43], focusing on the unit cells of C, Si, and Ge. Lattice parameters are optimized to 3.52 Å, 5.43 Å, and 5.65 Å, respectively, aligning with experimental lattice parameters [31] of 3.57 Å, 5.43 Å, and 5.67 Å. The structure optimization process involves relaxing the structure and atomic positions until the ionic forces and the total energy converge to predefined thresholds being 10^{-10} Ry/Bohr and 10^{-12} Ry, respectively. The *ab initio* DFT calculations [44,45] are employed to assess electronic properties, with a regular Monkhorst-Pack (MP) **k**-point grid $12 \times 12 \times 12$ in the first Brillouin zone (BZ), accompanied by a kinetic energy cutoff of 80 Ry for the plane-wave basis. Lattice dynamic properties and the e-ph perturbation potential are evaluated through density-functional perturbation theory (DFPT) calculations [46], using a coarse q-point grid of $6 \times 6 \times 6$. Subsequently, e-ph matrix elements and phonon-limited scattering rates, as well as phonon-limited hole mobility, can be evaluated within the software packages WANNIER90 [47] and EPW [44,45,48]. To accurately calculate intrinsic hole scattering within degenerate valence bands, the Fermi energy level is fixed at 0.3 eV above the valence band maximum (VBM). Considering the substantial influence of spin-orbit coupling (SOC) on the prediction of hole mobility [18,19,21], the SOC effect is consistently considered within our computations. Further calculation details are provided in Ref. [41].

III. RESULTS AND DISCUSSIONS

A. First-principles calculation-predicted hole mobilities

Figure 1 presents the predicted hole mobilities of diamond, Si, and Ge as a function of temperature by performing the first-principles calculations, alongside available experimental data [15,31,49–57]. Despite considering only phonon scattering and excluding other mechanisms such as ionized impurity, alloy, and carrier-carrier scattering, our calculations show reasonable agreement with experimental data across the entire investigated temperature range (100−600 K) for all three materials. This agreement suggests that phonon scattering is the dominant limiting factor for hole mobility within this temperature range. Our predictions thus provide an upper bound for hole mobility in these semiconductors. It is worth noting that a set of experimental data in diamond deviates from the remaining experimental and computational results at a temperature below 300 K. This discrepancy is likely due to scattering by ionized impurities, which are often introduced
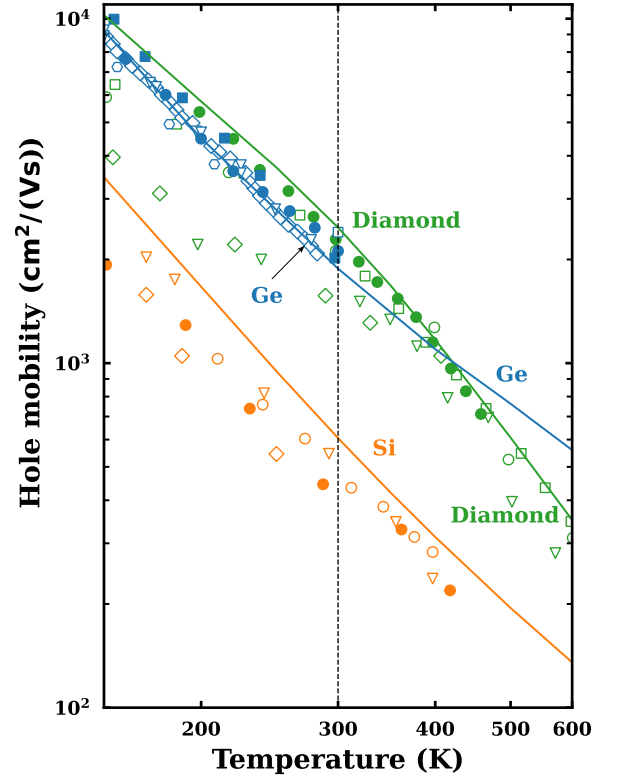

FIG. 1. Temperature dependence of hole mobilities in diamond (green), Si (orange), and Ge (blue). Solid lines represent theoretical calculations based on the first-principles approach. Experimental data points are shown for comparison: green points (diamond) from Refs. [31,49], orange points (Si) from Refs. [50–53], and blue points (Ge) from Refs. [15,54–58].

in lower-quality samples [31]. We observe that hole mobilities decrease exponentially with increasing temperature. From 200 to 600 K, mobilities reduce from 5752 to 350 cm^2/Vs in diamond, from 1667 to 135 cm^2/Vs in Si, and from 4496 to 559 cm^2/Vs in Ge. This decline is primarily attributed to the exponential increase in phonon population with temperature, as described by the Bose-Einstein distribution function, leading to enhanced scattering at higher temperatures. Notably, the hole mobility of Si remains consistently 4−5 times lower than that of both Ge and diamond across all temperatures. For example, at room temperature, hole mobility in Si is approximately 606 cm^2/Vs, whereas, in diamond and Ge, it is about 2470 and 1900 cm^2/Vs, respectively.

B. Role of extremely high light-hole mobility

According to Eq. (1), the total hole mobility at a given temperature is a sum of partial band mobilities of hh, lh, and split-off hole (sh) bands, weighted by their respective fractional occupation number. Figures 2(a)–2(c) show the total hole mobility and hh and lh partial band mobilities as a function of temperature in diamond, Si, and Ge, respectively. One can see that the lh partial mobilities μ_{lh} are notably higher than their hh counterparts μ_{hh}. Specifically, μ_{lh} is about 2.3 times [Fig. 2(a)] higher than μ_{hh} in diamond and 1.6 times higher in Si [Fig. 2(b)] within the entire investigated
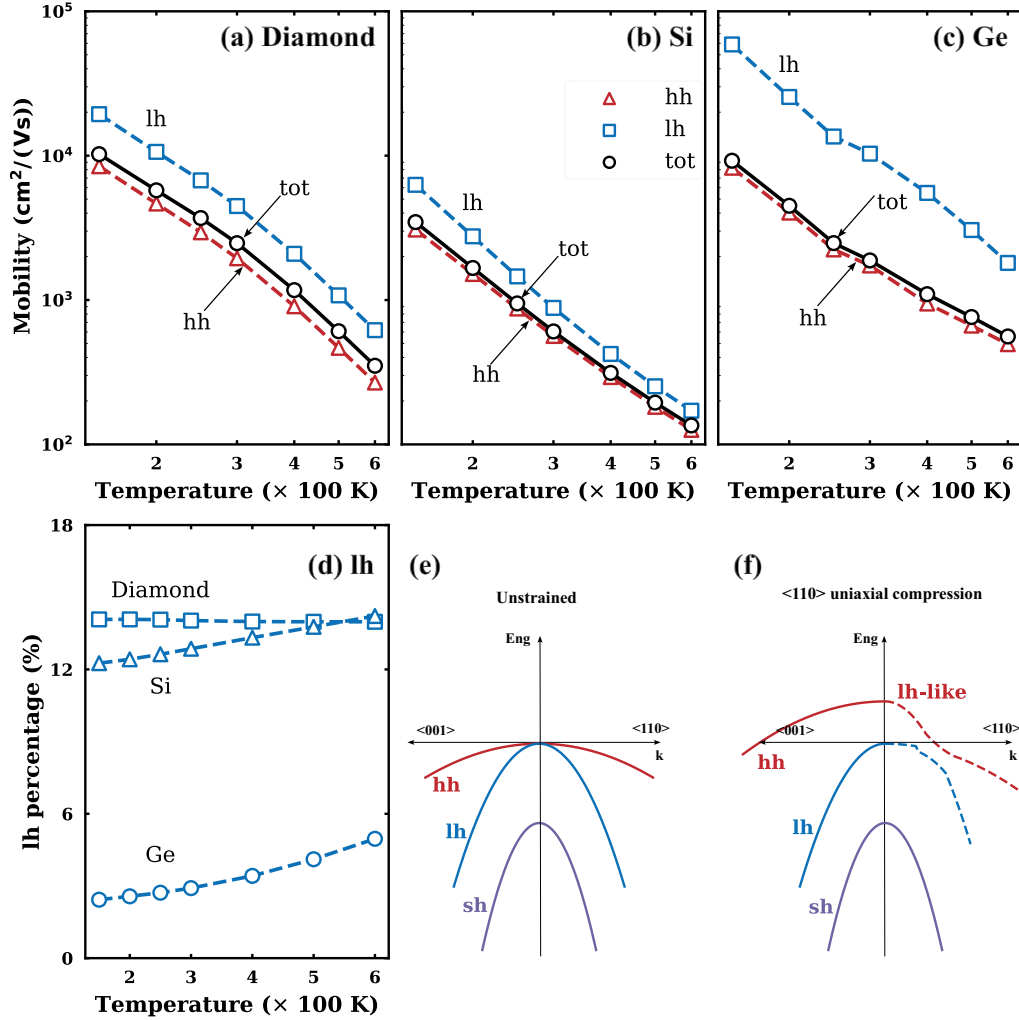
FIG. 2. (a)–(c) Temperature dependence of intrinsic hole mobilities for diamond, Si, and Ge, respectively. Total mobility (μ_{tot}, black solid line), heavy hole mobility (μ_{hh}, red solid line), and light hole mobility (μ_{lh}, blue solid line) are shown. (d) Temperature-dependent percentage concentration of light holes in diamond, Si, and Ge. Schematic representation of the valence band structure in bulk p-type Si (e) with the unstrained condition and (f) under ⟨110⟩ uniaxial compressive stress.

temperature range. Ge presents a particularly interesting case with μ_{lh} about an order of magnitude larger than its μ_{hh} [Fig. 2(b)]. This substantially higher μ_{lh} than μ_{hh} results in a remarkable enhancement of the total hole mobility despite the relatively low occupation of the lh band. At room temperature, the lh band occupation (o_{lh}) is only 20% in diamond, 14% in Si, and 3% in Ge at room temperature as shown in Fig. 2(d). This low occupation is attributed to the hh band's significantly smaller curvature in the energy dispersion compared to the lh band [Fig. 2(e)]. If holes were to exclusively occupy the hh band, then the total hole mobility would be determined by the hh partial hole mobility μ_{hh}, which is 1946 cm²/Vs for diamond, 560 cm²/Vs for Si, and 1630 cm²/Vs for Ge, respectively. However, considering the lh contribution at room temperature, the total hole mobility increases by 46 cm²/Vs in Si (from 560 to 606 cm²/Vs) and by approximately 250 cm²/Vs (from 1630 to 1880 cm²/Vs). These increases suggest that the lh contribution enhances room temperature hole mobility by 37.2% in diamond, 20% in Si, and 17% in Ge compared to the hh partial mobility. This significant

enhancement occurs despite the low lh band occupations of 20% in diamond, 14% in Si, and only 3% in Ge, respectively [Fig. 2(d)]. These findings underscore the crucial role of lh in determining the overall hole mobility in Group IV semiconductors and highlight potential strategies for mobility enhancement through band structure engineering by raising the lh occupation (or participation) in transport.

The contribution of the sh band to hole mobility is negligible regarding at room temperature the percentage of holes arising from the sh band decreases from 5.4% in diamond to 1.3% in Si and approaches near zero in Ge. This decreasing percentage is due to the stronger spin-orbit coupling (SOC) in heavier elements, which splits the sh band from the hh and lh bands at the Γ point by spin-orbit splitting Δ_{so} that increases from 13 meV in diamond to 44 meV in Si and 295 meV in Ge. Furthermore, holes from the sh band are mainly located around Γ point (see below), which has a heavy effective mass second to the hh band and thus low partial band mobility. Therefore, we do not show the sh band in Fig. 2 due to its negligible impact on hole mobility in the investigated

temperature range. Although strain can change the relative energy position between hh, lh, and sh and induce coupling between them, we note that the 44 meV energy separation in Si renders the sh band to barely influence the hole mobility by strains, as explicitly discussed in Sun's PhD thesis [59]. Of course, if Δ_{so} is small enough, like in diamond, then the sh band may affect the hole mobility, which will be discussed below.

Over the past three decades, strain engineering has been the leading technique to enhance transistor performance in the CMOS fabrication process by improving carrier mobility [39,40,59–65]. For instance, strain engineering in Si has been reported to increase the hole mobility in transistors by a factor of four compared to unstrained devices [39]. In 1963, Hasegawa [66] and Hensel and Feher [67] systematically studied the valence band effective masses and deformation potentials in strained Si based on the deformation potential theory with the **k** · **p** method. They identified key factors affecting hole mobility in semiconductors: band splitting and warping, effective mass change, and, consequently, the change of the density of states (DOS), which alters scattering final states and phonon scattering. It has been well documented that factors for strained mobility enhancement can be divided into two parts: (1) reduction in average conductivity effective mass caused by carrier repopulation and band warping and (2) suppression of interband scattering rate due to subband splitting and DOS changes [39]. The classical deformation potential theory has successfully explained experimentally observed changes in device behavior under mechanical stress and, to date, remains the primary method for modeling mobility in strained semiconductors [39]. We note that Kuhn [68] found that Ge PMOS transistors on (001) wafers exhibit a much larger enhancement in mobilities with increasing strain under a compressive ⟨110⟩ uniaxial stress relative to the Si PMOS transistors on (001) wafers. Hole mobility increases from approximately 430 to 940 cm^2/Vs in Ge PMOS, while it only increases from 200 to 300 cm^2/Vs in Si PMOS as strain increases from zero to 1.5 GPa. It is difficult to understand this substantial difference in strain-enhanced hole mobility between Ge and Si PMOS solely based on warping effects and effective mass changes. However, considering the significant difference in lh mobilities and the mixing of hh and lh states provides a straightforward explanation for this enhancement. As shown in Figs. 2(e) and 2(f), under ⟨110⟩ uniaxial compressive strain, the top band in bulk Si is lh-like along the channel and simultaneously hh-like out-of-plane [59]. Figure 2(b) demonstrates that a mere 1% rise in lh occupancy in Ge can lead to a mobility increase of up to 102 cm^2/Vs, whereas the increase is only 9 cm^2/Vs in Si. Consequently, introducing the same proportion of lh holes will improve hole mobility in Ge by nearly an order of magnitude more than in Si.

C. Hole-phonon scattering

We have to stress that the hh transport dominates in semiconductors at room temperature, as evidenced by the hh partial mobility (μ_{hh}) closely approximating the total hole mobility (μ_{tot}) across all temperatures in diamond, Si, and Ge, as shown in Figs. 2(a)–2(c). Therefore, understanding the mech-

anisms governing the hh partial mobility μ_{hh}, particularly the differences among diamond, Si, and Ge, is essential. To elucidate the origin of the difference in hh hole mobilities, we examine the scattering rates $1/\tau_{nk}$ of each hole state caused by longitudinal and transverse acoustic (LA and TA) phonons, as well as longitudinal and transverse optical (LO and TO) phonons at room temperature in diamond, Si, and Ge, respectively, as shown in Figs. 3(a)–3(c). For quantitative comparison, we calculate the average scattering rate $\langle 1/\tau \rangle$ over numerous hh states using Eq. (5) from our recent work [41], as presented in Fig. 3(d). Our analysis reveals that the average total scattering rate $\langle 1/\tau_{hh} \rangle$ in Si is approximately six times that in diamond and at least two times that in Ge. These significant differences in scattering rates provide a partial explanation for the observed variations in hh mobilities among these materials.

1. Remarkable transverse acoustic scattering

Figures 3(a)–3(c) reveal unexpectedly strong TA phonon scattering in diamond, Si, and Ge. This observation contradicts the common belief that TA phonons play a negligible role in hole-phonon scattering, as classical phenomenological models suggest LA phonons dominate due to their significant first-order effect on lattice spacing [69–74]. We recently uncovered the limitations in these classical phenomenological models in accurately capturing the strength of the TA-hole scattering matrix [41]. However, the material dependence of TA phonons' role in semiconductor transport remained ambiguous. Our results demonstrate that the relative importance of TA phonon scattering varies among the three materials. In diamond, TA scattering rates generally exceed LA scattering rates, while in Si, they are comparable, and in Ge, TA scattering rates become weaker than LA scattering rates. When summing the scattering rates of all initial states for a given phonon mode [Fig. 2(d)], TA scattering in Si is significantly stronger than in diamond and Ge. However, its contribution to the total acoustic scattering decreases from diamond to Ge, accounting for 62%, 51%, and 26% to the total acoustic scattering, respectively. According to Eq. (5), the scattering rate is approximately proportional to the square of the matrix elements $|g_{mnv}|^2$. The significant contributions of TA scattering in both diamond and Si can be attributed to their stronger TA-phonon-hole scattering matrix elements ($|g_{TA}|$) relative to LA-phonon-hole scattering matrix elements ($|g_{LA}|$), as shown in Figs. 4(a). Our first-principles calculations show that $|g_{TA}|$ (sum of the two TA branches) in diamond are considerably stronger than $|g_{LA}|$ along numerous **q** directions, except for the [111] direction. In contrast, $|g_{TA}|$ is comparable to $|g_{LA}|$ in Si and smaller than $|g_{LA}|$ in Ge.

To further illustrate the TA contribution, we extract the Bir-Pikus deformation potentials a_v, b, and d directly from the e-ph scattering matrix elements. These deformation potentials (a_v for hydrostatic as well as b and d for shear) are well-established parameters in the Bir-Pikus strain Hamiltonian model [75] and, thus, can be used to describe the strength of hole-acoustic-phonon scattering. We first derive **k**-dependent deformation potential $D_{mnv}(\mathbf{k}, \mathbf{k} + \mathbf{q})$ from the first-principles scattering matrix elements $|g_{mnv}|$ through $D_{mnv}(\mathbf{k}, \mathbf{k} + \mathbf{q}) = \sqrt{\frac{2M_0 \omega_{vq}}{\hbar}} g_{mnv}(\mathbf{k}, \mathbf{k} + \mathbf{q})$ [41] (here, M_0 is the total atomic
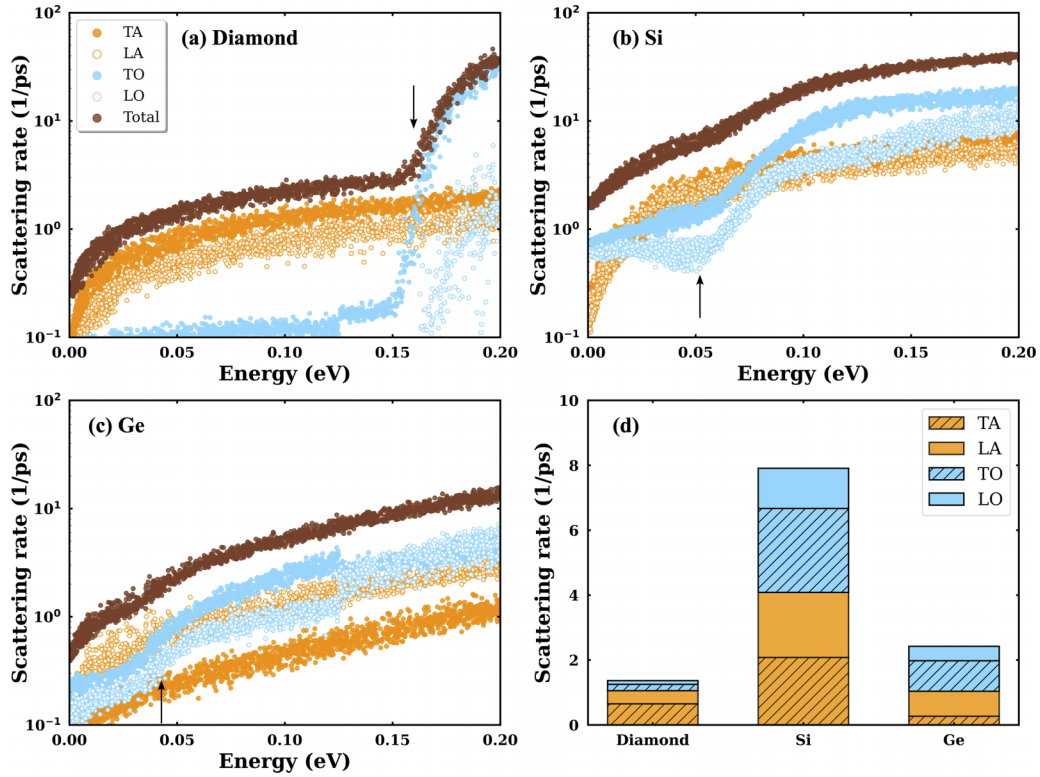
FIG. 3. Decomposed scattering rate of heavy holes into different phonon branches at room temperature for (a) diamond, (b) Si, and (c) Ge, respectively. (d) The average scattering rate of the heavy hole for diamond, Si, and Ge. Orange-filled dots indicate two transverse acoustic modes, TA (TA1 and TA2); Orange-open dots indicate the longitudinal acoustic mode, LA; Cyan-filled dots indicate two transverse optical modes, TO (TO1 and TO2); Cyan-open dots indicate the longitudinal optical mode, LO.

mass of the unit cell, and $\omega_{v\mathbf{q}}$ is phonon frequency related to the phonon with the branch index v and wave vector $\mathbf{q}$). Note that $D_{mnv}(\mathbf{k}, \mathbf{k} + \mathbf{q})$ is proportional to the overlap between the initial and final scattering electronic states and hence inversely scales with the square of bond length, $1/d^2$. For the long-wavelength scattering, we quantify the complex function of angle- and $\mathbf{k}$-dependent deformation potential $D_{mnv}(\mathbf{k}, \mathbf{k} + \mathbf{q})$ using acoustic deformation potential constants: $\Xi_{v,\theta} = \lim_{\mathbf{q}\to 0} |\frac{D_{mnv}(\mathbf{k},\mathbf{k}+\mathbf{q})}{\mathbf{q}}|$ for $\mathbf{k}$ along the [100] direction, where θ is the angle between the phonon wave vector $\mathbf{q}$ and the principal axis $\mathbf{k}$. We then extract the Bir-Pikus deformation potentials a_v, b, and d by fitting $\Xi_{v,\theta}$ according to Eq. (15) in Ref. [41]. It is important to note that the deformation potential a_v cannot be determined from band changes under pressure, either experimentally [71,76,77] or theoretically [78–80], as only relative energies between bands, rather than absolute energies of individual bands, can be obtained. Both b and d (representing the splitting of $\Gamma_{25'}$ valence states by uniaxial stresses along the [110] and [111] directions, respectively) can be obtained from the measured dispersion of the piezooptical constants [81]. However, reported values [15,25,26,69,71,81–84], as shown in Table I, exhibit significant divergences and even opposite signs.

Our extracted Bir-Pikus deformation potentials a_v, b, and d are summarized in Table I in comparison with previously reported values [15,25,26,69,71,81–84]. For Si and Ge, our calculated a_v values (2.37 and 3.69 eV, respectively) fall within the range of literature values, and the extracted b and

d values show good agreement with the previously reported data. However, for diamond, our extracted a_v (3.45 eV) differs significantly from literature values (e.g., 7 and -36.1 eV) [15,81,82,84], and b also shows notable discrepancies. Importantly, our directly extracted a_v are all positive, in sharp contrast to the negative values reported for diamond in several studies [15,81,82,84]. This positive a_v can be attributed to the p-orbital bonding nature of the $\Gamma_{25'}$ valence band edge, which typically shift upward in energy with increasing bond length (or volume expansion). Our extracted a_v values reasonably agree with previous first-principles calculations based on valence band edge shifts under volume deformation [85]. Furthermore, our predicted effective deformation potential E_{ADP} (defined in the footnote of Table I) shows good agreement with values obtained by fitting experimentally measured temperature-dependent hole mobilities. This consistency lends credibility to our approach while highlighting uncertainties in our current understanding of dilation deformation potentials and microscopic scattering mechanisms in diamond.

2. Abnormally high hole-optical-phonon matrix elements in diamond

It is commonly believed that the highest hole mobility in diamond is attributed to the longest momentum relaxation times by overcoming its heaviest effective mass among group IV semiconductors [26–28]. The longest momentum relaxation time in diamond results from the much higher velocity
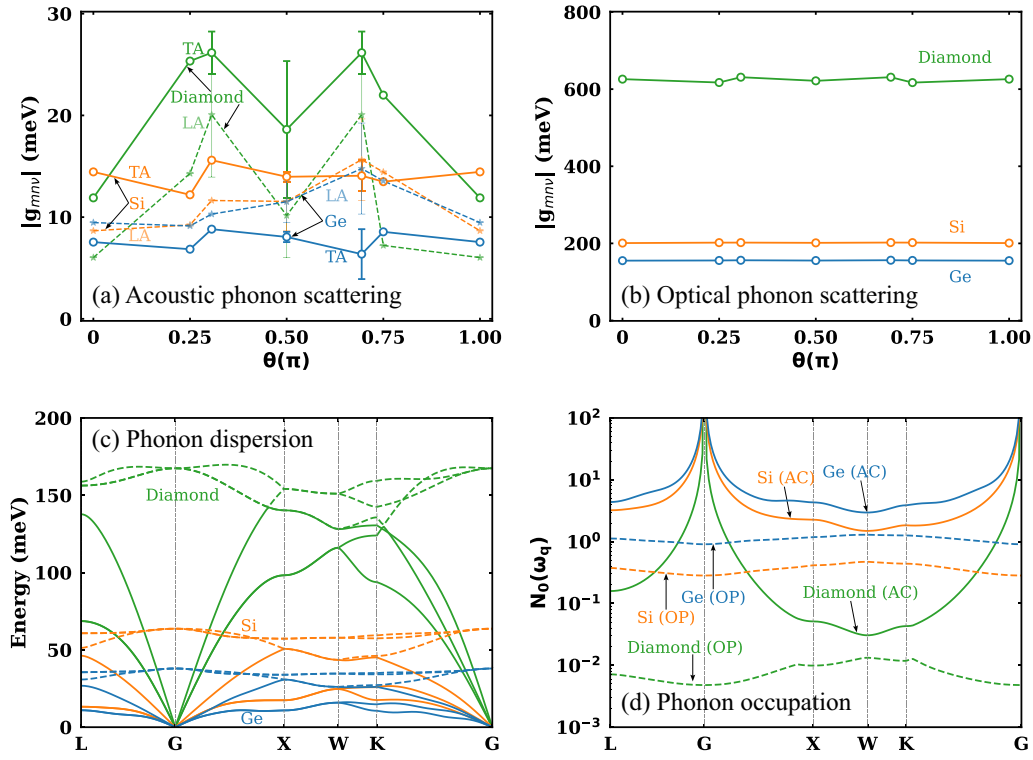
FIG. 4. (a) Angular dependence of the electron-phonon scattering matrix elements $|g|$ for holes near the valence band maximum (VBM) interacting with transverse acoustic (TA) and longitudinal acoustic (LA) phonons in diamond, Si, and Ge. The scattering angle θ is calculated relative to the [100] direction. (b) Angular dependence of $|g|$ for optical phonons in diamond, Si, and Ge. (c) Phonon dispersion and (d) phonon occupation along high-symmetry directions for diamond (green), Si (orange), and Ge (blue). Solid lines represent acoustic (AC) modes, while dashed lines indicate optical (OP) modes.

TABLE I. Extracted Bir-Pikus and effective acoustic deformation potentials for the hole-acoustic-phonon scattering for diamond, Si, and Ge. Note all the deformation potentials are in the unit of eV.

		Diamond	Si	Ge
a_v (eV)	Present work	3.45	2.37	3.69
	Literature	−36.1[a, b], 7.1[c], −8[c], −13.9[c], −35.1[d]	−5[a], 10.2[b], 2.1[e, f], 2.46[f], 2.06[f]	−5.2[a], 12.4[b], 2.0[e, f], 1.24[f], 2.09[f], −12.7[f], 1.39[f]
b (eV)	Present work	−2.36	−1.87	−1.4
	Literature	−11.1[a, b], −8.1[b], −4.67[c], −4.99[c], −17.8[d]	−2.3[a, b], −3.0[b], −2.2[b, f], −8.7[b], −3.5[b], −5[b], −2.2[b], −1.5[e], −2.33[f], −1.5[f], −2.1[f], −2.12[f], −2.35[f], −2.58[f], −2.27[f]	−2.4[a], −3.1[b], −2.3[b], −3.2[b], −2.2[e, f], −2.16[f], −2.1[f], −2.08[f], −2.5[f], 2.86[f], −3.11[f]
d (eV)	Present work	−4.53	−3.6	−2.51
	Literature	−5.42[b], 3.7[b], 2.7[b], −3.80[c], −1.63[c], −15.6[d]	−5.3[a], −8.7[b], −7.2[b], −5.1[b], −3.9[b], −5.5[b], −3.4[f], −4.85[f], −5.3[f], −3.69[f]	−4.8[a], −7.2[b], −5.6[b], −5.0[b], −4.4[e], −3.5[f], −4.4[f], −3.7[f], −4.5[f], −5.3[f], −4.65[f], −7.0[f]
E_{ADP}[j] (eV)	Present work	5.44	4.37	3.98
	Literature	5.65[g],	2.8[e], 3.7[e], 5.39[f], 3.1[f], 5.0[f], 6.2[f], 3.54[g, h], 2–3[i]	3.5[e], 7.9[e], 6.49[f], 3.66[f], 4.6[f],

[a]Reference [15]; [b]Reference [82]; [c]Reference [84]; [d]Reference [81]; [e]Reference [83]; [f]Reference [25] and references therein; [g]Reference [26]; [h]Reference [69]; [i]Reference [71]; [j]$E_{\mathrm{ADP}}^2 = \frac{\beta+2}{3\beta} \times [a^2 + \beta(b^2 + \frac{1}{2}d^2)]$, where $\beta = c_l/c_t$, and the average longitudinal and transverse elastic constants are $c_l = (3c_{11} + 2c_{12} + 4c_{44})/5$, and $c_t = (c_{11} - c_{12} + 3c_{44})/5$ [25] with the elastic constants c_{11}, c_{12}, and c_{44} from Ref. [31].

of the longitudinal acoustic phonons and the higher optical phonon energy, significantly reducing the number of phonons participating in carrier scattering [27]. As shown in Fig. 3, the optical phonon scattering rates in the diamond [Fig. 3(a)] remain exceptionally low compared to Si [Fig. 3(b)] and Ge [Fig. 3(c)] until hole energy reaches about 0.16 eV. Beyond this threshold, there is an abnormally sharp increase of two orders of magnitude. This sharp transition in optical phonon scattering rates is absent in both Si and Ge, where only minor kinks are observed at 0.06 and 0.04 eV, respectively. To understand this phenomenon, we examine the phonon dispersion of the diamond, Si, and Ge, as shown in Fig. 4(c). The optical phonon frequency in the diamond ($\hbar\omega_o \approx 167$ meV) substantially exceeds that of Si (around 64 meV) and Ge (around 38 meV). Consequently, as shown in Fig. 4(d), the room-temperature occupation number of optical phonons in diamond is approximately 0.01, two orders of magnitude lower than that in Si and Ge, and at least three orders of magnitude below its acoustic counterparts. Surprisingly, the average optical phonon scattering rate τ_{ODP} in the diamond is finite, reaching about 10% of that in Si, and optical phonon scattering contributes 23% of the total hole-phonon scattering in diamond [Fig. 3(d)]. This unexpected behavior stems from diamond's significantly larger hole-optical-phonon scattering matrix elements. As illustrated in Fig. 4(b), the hole-optical phonon scattering matrix elements in diamond (≈ 624 meV) far exceed those in Si (≈ 201 meV) and Ge (≈ 155 meV). Since carrier-phonon scattering rates are proportional to the square of scattering matrix elements, the ninefold stronger square of hole-optical phonon scattering matrix elements in diamond compared to Si accounts for the finite optical scattering rates despite diamond's negligible optical phonon occupation at room temperature.

The extremely large hole-optical phonon scattering matrix elements in diamond are also responsible for the sharp rise in the hole-optical scattering rates with energy above 0.16 eV, as shown in Fig. 3(a). In the low-energy region ($\varepsilon_{n\mathbf{k}} < \hbar\omega_o$), the interaction between optical phonons and hh holes is predominantly governed by the phonon absorption process. Phonon emission processes are forbidden due to the absence of available scattering final states in the satisfaction of the energy conservation law. Consequently, optical phonon scattering rates in this low-energy regime are proportional to the occupation number of optical phonons $N_{op,\mathbf{q}}$ and exhibit an almost energy-independent, as illustrated in Figs. 3(a)–3(c). As hole energy surpasses the optical-phonon energy ($\hbar\omega_o$), the optical phonon emission becomes energetically permissible. The scattering rates of the emission processes are proportional to $(1 + N_{op,\mathbf{q}})$, rather than $N_{op,\mathbf{q}}$ (≈ 0.01), resulting in significantly higher scattering rates compared to the absorption processes. As shown in Fig. 4, the optical phonon scattering matrix elements $|g_{op}|$ exceed acoustic phonon scattering matrix elements $|g_{ac}|$ by two orders of magnitude. Given that phonon scattering rates are also proportional to the square of the scattering matrix elements, optical phonon scattering dominates over acoustic phonon scattering once the optical phonon emission processes are allowed [26–28]. Consequently, despite the high optical phonon frequency in diamond significantly reducing the number of phonons participating in carrier scattering, the extremely strong hole-

optical-phonon scattering matrix elements efficiently scatter high-energy holes through emission processes. This mechanism contributes up to 23% of the total scattering rate at room temperature in the diamond.

The extremely large hole-optical phonon scattering matrix elements in diamond also account for the distinctive kink observed in the temperature-dependent hole mobility, as shown in Fig. 1. At low temperatures, only low-energy hole states are thermally occupied and contribute to transport. In this regime, acoustic phonon scattering predominantly governs the hole mobility. As temperature rises, high-energy hole states become thermally activated and participate in transport processes. A critical transition occurs when holes with energies exceeding about 0.16 eV, capable of optical phonon emission, become increasingly involved in transport. At approximately 400 K, these high-energy holes contribute substantially to hole transport, leading to a dominance of optical phonon scattering over acoustic phonon scattering. This transition manifests as a distinct kink in the temperature-dependent hole mobility curve for diamond at 400 K, as shown in Fig. 1. Our findings also align with the observations of Akimoto *et al.* [28], who similarly concluded that optical phonon processes become the dominant carrier scattering mechanism in diamond above 400 K.

3. Crucial rule of effective mass

While phonon characteristics significantly influence carrier mobilities, effective mass remains a critical determinant of mobility. In the preceding section, we demonstrated that diamond exhibits a remarkable suppression of phonons involved in hole scattering. This phenomenon leads to an outcome that diamond exhibit the the highest hole mobility among group IV semiconductors despite having the heaviest effective mass according to the common perception [26–28]. Figures 4(b)–4(g) show that Si and Ge exhibit comparable values in scattering matrix elements and phonon occupations at room temperature. This similarity implies that effective mass is dominant in explaining the approximately fourfold higher hole mobility in Ge compared to Si. The relationship between effective mass and carrier mobility can be understood through Eq. (2), where effective mass directly regulates carrier mobility via the group velocity of each electronic state with energy $\varepsilon_{n\mathbf{k}}$ [86],

$$v_{n\mathbf{k},\alpha}v_{n\mathbf{k},\beta} = 2\varepsilon_{n\mathbf{k}}/m^*_{n\mathbf{k},\alpha\beta}, \qquad (6)$$

where $m^*_{n\mathbf{k},\alpha\beta}$ represents the effective mass tensor. Neglecting nonparabolic and warping effects of the energy band ($m^*_{n\mathbf{k},\alpha\beta} = m^*_n$), as often assumed in phenomenological scattering models [86], we can further simplify this relationship using a single value of effective mass m^*_n for band n: $m^*_n = \int m^*_{n,k} \cdot f^0_{hh,\mathbf{k}}(\mathbf{k}) \cdot d\varepsilon_{n,\mathbf{k}}$. Consequently, the hh mobility in Eq. (2) can be approximated as $\mu_{hh} = e\tau_{hh}/m^*_{hh}$, aligning with the Drude formula [29]. Here, m^*_{hh} and τ_{hh} represent the effective mass [29] and scattering relaxation time of the hh band, respectively.

Using first-principles calculation of the group velocity $v_{n\mathbf{k}}$ and eigenvalue $\varepsilon_{n\mathbf{k}}$, we can deduce the average hh effective mass by $m^*_{hh,k\text{-ave}} = \int m^*_{hh,k} \cdot f^0_{hh,\mathbf{k}} \cdot d\varepsilon_{hh,k}$, where $m^*_{hh,\mathbf{k}}$ is the $\mathbf{k}$-dependent hh effective mass. It is important to distinguish this average effective mass $m^*_{hh,k\text{-ave}}$ from the conventional

TABLE II. Comparison of diamond's heavy-hole (hh) masses: Experimental measurements versus theoretical calculations. $m^*_{hh,c}$ is the conductivity mass defined in Ref. [86]. m_{curv} represents that hole masses obtained from the curvature of the hh band using the finite difference method with a five-point stencil [87] with a step size of $h = 0.01$/Bohr. $m_{k\text{-avg}}$ represents that hole masses are calculated by $m^*_{hh} = \int m^*_{hh,\mathbf{k}} \cdot wt(\mathbf{k}) \cdot d\varepsilon_{hh,\mathbf{k}}$ with weight factor $wt = f^0_{hh,\mathbf{k}}$. The hole effective masses of the first three rows are calculated along [100], [110], and [111] directions using valence band parameters A, B, and C (or Luttinger parameters) reported in Refs. [15,29,31]. All masses are in units of the free-electron mass (m_0).

	Ref.	$m^{*[100]}_{hh}$	$m^{*[110]}_{hh}$	$m^{*[111]}_{hh}$	$m^*_{hh,c}$
	Ref. [15]	0.3846	0.7905	1.2195	0.640
	Ref. [31]	0.2915	0.5076	0.6741	0.436
Theory	Ref. [29]	0.4348	0.6626	0.8028	0.594
	Ref. [88]	0.40, 0.36, 0.32, 0.366	1.34, 1.48, 1.39, 1.64, 1.783	0.56, 0.67, 0.65, 0.65	0.58±0.02
	Ref. [89]	0.427	0.69	0.778	0.591
	Ref. [90]	0.36–0.42			
Expt.	Ref. [91]	0.54	0.7	0.76	0.653
	Ref. [92]	0.51	1.47	2.22	0.970
Others,	Ref. [15,29–33,93,94]		0.4, 0.53, 0.66, 0.78, 1.07, 1.08, 2.12, 2.13, 2.30		
This work	$m_{curv}(0.01)$	0.418	0.723	0.677	0.571
	$m_{k\text{-avg}}$	0.3941	1.1918	0.7018	0.625

effective mass (m^*_{curv}). The former represents a collective property of the electronic states, while the latter is defined for a single electronic state, e.g., at the Γ point. Tables II, III, and IV compare our extracted hh effective masses for diamond, Si, and Ge with theoretical and experimental data from the literature. Our deduced hh conductivity effective masses m^*_{hh} are about $0.5 \pm 0.05\ m_0$ for Si and $0.35 \pm 0.03\ m_0$ for Ge, aligning well with commonly quoted values [15,21,29–32], e.g., $0.54\ m_0$ in Si and $0.34\ m_0$ in Ge [29]. Scattering rate $1/\tau_{hh}$ is the sum of scattering lifetimes $\tau_{hh,\mathbf{k}}$ of all sampled $\mathbf{k}$-states weighted by their occupation number for a hole located inside the $n = hh$ band, as defined in Eq. (5). It is straightforward to learn that the effective mass also regulates the hh mobility through the scattering time by quantifying the density of final states, as ensured by the energy-conserving Dirac delta function. This effective mass, appearing in the scattering time, is termed the density of state effective mass [29]. According to the phenomenological deformation potential theory [29,30,43,86], both acoustic and optical scattering times scale

with the density-of-states effective mass as $\tau_{hh} \propto (m^*_{hh})^{-3/2}$ (Note that we temporarily ignore the difference between conductivity and density-of-states effective mass). Therefore, the hh hole mobility μ_{hh} should scale as $\propto (m^*_{hh})^{-5/2}$. The ratio $[m^*_{hh}(Si)/m^*_{hh}(Ge)]^{5/2} \approx 3.0$ is now of the same magnitude as the corresponding hh mobilities $\mu_{hh}(Ge)/\mu_{hh}(Si)$, underscoring the crucial role of a light effective mass to have a high hole mobility.

However, the reported hh effective mass in diamond exhibits significant variability, ranging from $0.4\ m_0$ to $2.30\ m_0$ [15,29–33]. This wide distribution, including values such as $0.66\ m_0$ [29], $0.78\ m_0$ [15], $0.53\ m_0$ [30], $1.08\ m_0$[31], $2.12\ m_0$ [32], $2.30\ m_0$ [33], underscores the significant uncertainty in diamond's hole effective mass. Here, our first-principles calculation yield the hh effective mass in diamond to be approximately $0.6 \pm 0.03\ m_0$, aligning with the lower values (e.g., both $0.53\ m_0$ and $0.66\ m_0$) reported in the literature [29,30]. Considering the relationship $\mu_{hh} \propto (m^*_{hh})^{-5/2}$, the experimentally reported mass $2.30\ m_0$ [33] instead of our

TABLE III. Comparison of Si's heavy-hole (hh) masses: Experimental measurements versus theoretical calculations.

		$m^{*[100]}_{hh}$	$m^{*[110]}_{hh}$	$m^{*[111]}_{hh}$	$m^*_{hh,c}$
	Ref. [15]	0.2772	0.5137	0.7179	0.432
	Ref. [31]	0.2747	0.5192	0.7381	0.433
	Ref. [29].	0.2778	0.5186	0.7294	0.435
Theory	Ref. [95]	0.26	0.54	0.67	0.417
	Ref. [96]	0.312	0.609	0.75	0.485
	Ref. [97]	0.346	0.618	0.732	0.511
	Ref. [21]	0.271, 0.276, 0.256, 0.243,	2.158, 2.170, 2.868, 0.521, 0.512,	0.635, 0.678, 0.694, 0.654, 0.643	0.47±0.07
	Ref. [98]	0.46	0.53	0.56	0.513
Expt.	Ref. [99]	0.46	0.53	0.56	0.513
	Ref. [100]	0.46	0.53	0.57	0.516
	$m_{curv}(0.01)$	0.26036	0.54674	0.66053	0.418
This work	$m_{curv}(0.08)$	0.27915	2.03484	0.74875	0.555
	$m_{k\text{-avg}}$	0.2729	2.4772	0.7317	0.552

TABLE IV. Comparison of Ge's heavy-hole (hh) masses: Experimental measurements versus theoretical calculations.

		$m_{\text{hh}}^{*[100]}$	$m_{\text{hh}}^{*[110]}$	$m_{\text{hh}}^{*[111]}$	$m_{\text{hh},c}^{*}$
	Ref. [15]	0.2041	0.367	0.5	0.312
	Ref. [31]	0.2114	0.3737	0.5022	0.319
Theory	Ref. [29]	0.2049	0.3695	0.5046	0.314
	Ref. [101]	0.226	0.439	0.597	0.358
	Ref. [96]	0.251	0.467	0.623	0.388
	Ref. [97]	0.254	0.477	0.39	0.349
Expt.	Ref. [100]	0.284	0.352	0.376	0.333
This work	$m_{\text{curv}}(0.01)$	0.20469	0.3838	0.52355	0.319
	$m_{k\text{-avg}}$	0.2179	0.6328	0.5378	0.374

calculated value would give rise to an ultralow hole mobility $\mu_{\text{hh}} \approx 70$ cm^2/Vs, even diamond owns the unique phonon characteristics that were regarded to be the main reason to have high hole mobility. Figure 5(a) shows that an effective mass of 2.30 m_0 for diamond is reasonable given that its fundamental band gap is $E_g = 5.50$ eV [31], which is almost five times that of Si ($E_g = 1.12$ eV) [31]. This comparison suggests that our calculated low effective mass for diamond is anomalous, considering the general trend of increasing effective mass with increasing bandgap in semiconductors.

The deviation of the hh effective mass from the free-electron mass m_0 is primarily attributed to $\mathbf{k} \cdot \mathbf{p}$ coupling
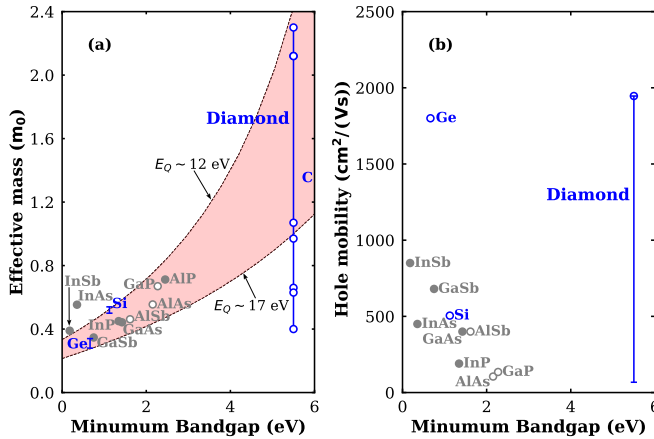

FIG. 5. (a) Heavy hole effective mass (m_{hh}^{*}) as a function of the minimum bandgap (E_g) for a range of semiconductor materials. The relationship between m_{hh}^{*} and E_g is described by the $\mathbf{k} \cdot \mathbf{p}$ [102]: $\frac{1}{m_{\text{hh}}^{*}} = \frac{1}{m_0}(1 - \frac{E_Q}{E_g + \Delta E})$. Here, energy term ($E_g + \Delta E$) represents the bandgap Γ_{15v} and Γ_{15c} with the assumption of E_g approximate to minimum bandgap and $\Delta E \approx 3$ eV [103], and E_Q represents the energy related to momentum matrix elements between Γ_{15v} and Γ_{15c} states, typically in the range of $\sim 12-17$ eV [29,103]. Data points are obtained from Refs. [31,32], with group IV semiconductors represented by ranges reported in literature [15,26,29,32,33]. (b) Bulk hole mobility versus minimum bandgap for various semiconductor materials, including group IV, III–V, and II–VI compounds [31]. Filled symbols denote direct bandgap semiconductors, while open symbols represent indirect bandgap materials. Note the exceptional hole mobilities of Ge and diamond among known semiconductors.

between the zone-center state Γ_{15v} (for zincblend (ZB) crystals or $\Gamma_{25'v}$ for diamond crystals) and the *p*-orbital antibonding states Γ_{15c} (Γ_{15c} for diamond crystals) since it does not couple to the conduction *s* electron Γ_{1c}. Within the $\mathbf{k} \cdot \mathbf{p}$ approximation, the isotropic hh effective mass is approximated as $\frac{1}{m_{\text{hh}}^{*}} = \frac{1}{m_0}(1 - E_Q/E_0')$ [102], where E_0' ($\approx E_g + \Delta E$) denotes the energy separation between Γ_{15c} and Γ_{15v} for ZB and Γ_{25v} for diamond structure, and $E_Q = 2Q^2/m_0$ is the energy associated with the momentum matrix element Q between these two states. E_Q is often considered material-independent [29] and typically falls within the range of $\sim 12-17$ eV [29,103]. With the well-documented $E_0' = 3.4$ eV in Si and $E_0' = 7.3$ eV in diamond [31], assuming diamond has the same E_Q as Si (takes Si hh effective mass $m_{\text{hh}}^{*} = 0.54 \, m_0$ as a reference), diamond's expected hh effective mass would be $m_{\text{hh}}^{*} = 2.5 \, m_0$, which supports the largest reported value of 2.30 m_0 in diamond [33]. Changing diamond's hh effective mass from our calculated value to the reported value $m_{\text{hh}}^{*} = 2.30 \, m_0$ would dramatically reduce the hh hole mobility from 1940 cm^2/Vs to 70 cm^2/Vs, which is even nine times lower than that in Si. Consequently, diamond's anomalously low hh effective mass is crucial for its high hole mobility of 1940 cm^2/Vs. This finding challenges the common belief that diamond's high intrinsic mobility results from its high phonon frequency, which was thought to produce a very long scattering time, overcoming the heaviest effective masses to yield the highest hole mobility [26–28].

To understand why the diamond has an abnormally small hh effective mass, we examine the interband momentum matrix element Q. This element, representing the wavefunction overlap between initial and final scattering electronic states, scales inversely with the square of the lattice constant *a* (or bond length). According to the dipole approximation [104–106], Q is related to oscillator strengths, which satisfy the sum rule [106] and are proportional to the effective concentration of valence electrons, N_{eff}. Notably, the effective concentration of valence electrons differs among diamond, Si, and Ge. While diamond and Si lack *d*-electrons, Ge possesses a fully occupied *d* orbital with 10 semi-core *d*-electrons that partially contribute to the valence electrons. This contribution is quantified by the parameter $D = N_{\text{eff}}/N$, first introduced by Van Vechten [105], where N is the number of *s* and *p* valence electrons. For diamond and Si, $D = 1$, whereas for Ge, $D > 1$. As atomic number increases, the lattice constant
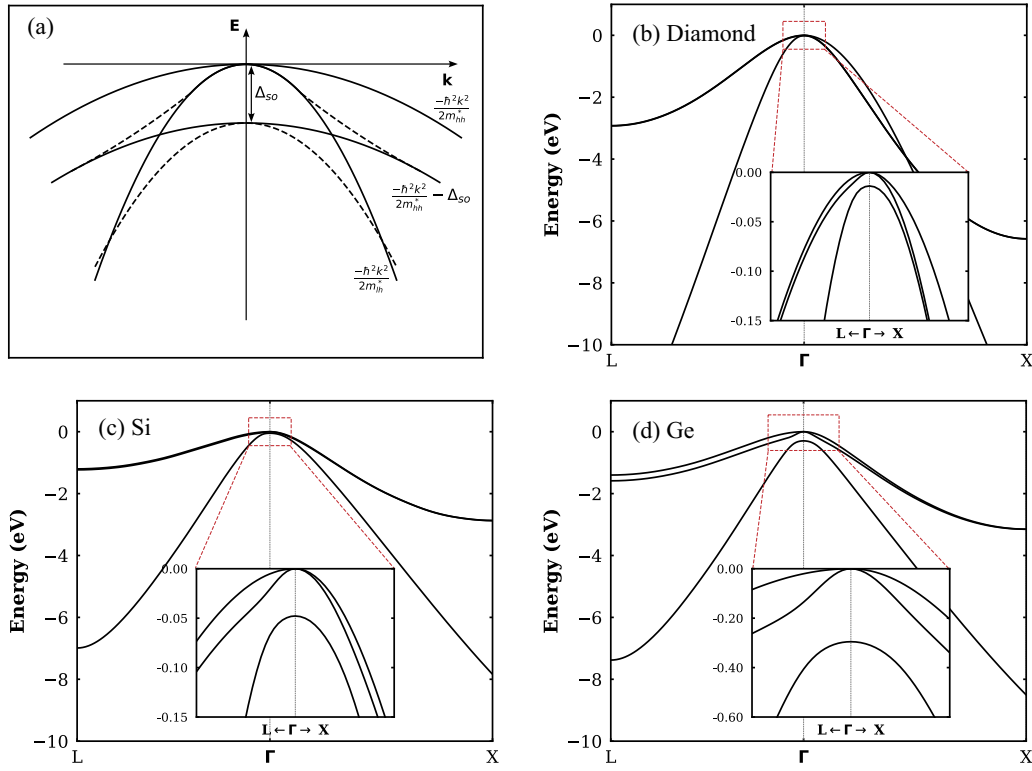
FIG. 6. Valence band structures of diamond-structure semiconductors. (a) Schematic representation of the nonparabolic valence band structure in diamond-structure materials with spin-orbit coupling. Spin-orbit coupling splits off one of the otherwise degenerate heavy-hole bands, as shown by the lowest black solid line. The split heavy-hole (hh) band then becomes mixed with the light-hole (lh) band to give final energy bands, as shown by the dashed lines. (b)–(d) First-principles calculations of valence band structures along the L-Γ-X high-symmetry path in the Brillouin zone for (b) diamond, (c) Si, and (d) Ge. The lower-center inset shows a magnified view of the band structure near the Γ point.

a and the d-electron enhancement tend to increase. These effects partially compensate each other, often resulting in a material-independent Q [102,104]. Lawaetz [104] has approximated E_Q [relative to $E_Q(\text{Si})$ in Si] by considering these two critical factors as follows:

$$E_Q = \frac{2Q^2}{m_0} \approx E_Q(\text{Si})\eta, \quad \text{with}$$

$$\eta = [1 + 1.23(D - 1)](a_{\text{Si}}/a)^2. \tag{7}$$

Interestingly, Si exhibits an E_Q similar to that of many common semiconductors, including III–V and II–VI semiconductors [104]. Ge, due to the presence of d-electrons, has a larger E_Q (26.3 eV). When combined with Ge's smaller E_0', this results in an effective hole mass approximately half that of Si. Diamond presents a unique case. Although it shares the absence of d-electrons with Si ($D = 1$), diamond's much smaller lattice constant (35% shorter than Si) leads to a significantly larger scaling factor η. This dramatically increases E_Q to 49.8 eV in diamond, more than twice that of Si. Consequently, diamond maintains a comparable effective mass to Si, despite its E_0' bandgap being twice as large as Si's.

Additionally, Figs. 6(b)–6(d) present the valence band structure along the Γ-L and Γ-X directions for diamond, Si, and Ge, respectively. In Si and Ge, away from the Γ point, the energy dispersions of the top two valence bands (named hh and lh bands) are almost parallel along both directions,

while the sh band exhibits the greatest curvature (or smallest effective mass). In diamond, however, this pattern holds true along Γ-L but not along Γ-X, where the top valence band is isolated from the remaining two parallel bands, as shown in Fig. 6(a). To understand this phenomenon, we first examine the valence band structure in the absence of SOC [107]. Without SOC, the top two bands are degenerate hh bands with identical effective masses, while the lowest band is the lh band with the greatest curvature (or smallest effective mass) due to its additional coupling to the s-like conduction band. The introduction of SOC splits the double-degenerate bands by shifting one down by an energy of Δ_{so} to form the sh band with the same effective mass as the hh band. The high-lying lh band would cross the low-lying sh band at a certain k-point due to its greater curvature if they were not coupled. However, the $\mathbf{k} \cdot \mathbf{p}$ term introduces strong coupling between the sh and lh bands, resulting in anticrossing, as schematically shown in Fig. 6(a), since their off-Γ states share the same symmetry. This strong coupling causes the low-lying band to have the smallest effective mass at the off-Γ point. After the anticrossing as $\mathbf{k}$ moves away from the Γ point, the sh band becomes parallel to the hh band due to their similar effective mass, while the lh band becomes the lowest one in energy. In this context, we have to label the top two parallel bands as hh, and sh bands, with their energy separation being approximately $\frac{2}{3}\Delta_{\text{so}}$ [108], and the low-lying band as the lh band [107], different from the common nomenclature. In diamond, the
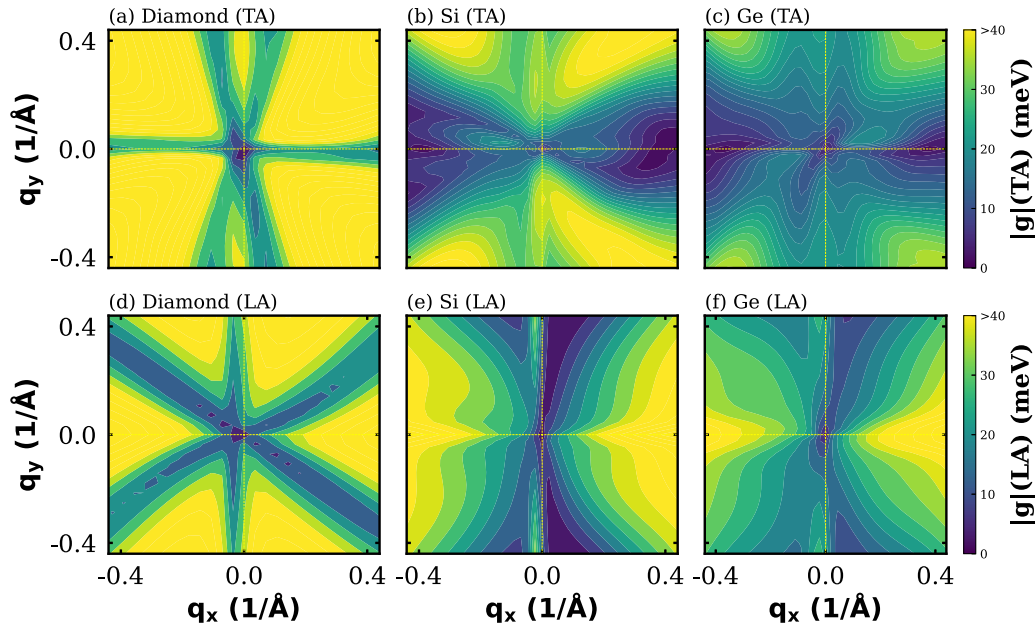
FIG. 7. The contour maps of hole-phonon scattering matrix elements $g_{mnv}(\mathbf{k}, \mathbf{k} + \mathbf{q})$ in the q_x-q_y plane of the Brillouin zone for (a) diamond, (b) Si, and (c) Ge. The maps are presented for $q_z=0$, with the initial hole state $|n, \mathbf{k}\rangle$ located at the valence band maximum (VBM).

small $\Delta_{so} = 13$ meV allows the strong $\mathbf{k} \cdot \mathbf{p}$-induced lh/sh coupling near the Γ point to elevate the lh band above the hh band along the Γ-X direction, making the lh band be the highest valence band, with the hh and sh bands parallel below it. Consequently, diamond's top band is hh along the Γ-L direction and is lh band along the Γ-X, resembling the valence band structure in uniaxially strained Si and Ge, as depicted in Fig. 2(f). This unique feature is further corroborated by the distinct scattering matrix element patterns of TA and LA phonons in diamond compared to Si and Ge, as shown in Fig. 7. Edmonds *et al.* [90] reported a band effective mass of only 0.36–0.4 m_0 along Γ-X direction via normal emission angle-resolved photoemission spectroscopy, in contrast to the reported values of 2.0 and 2.13 m_0 from cyclotron resonance measurements. This discrepancy supports our findings and suggests that diamond's high hole mobility partially stems from its unique valence band structure, featuring an admixture of hh and lh characteristics, which has been utilized to enhance the hole mobility in the transistor.

4. Role of interband scattering in multiband model

The preceding discussion primarily focuses on hole scattering within a single band, an approximation commonly employed in classical phenomenological approaches [26–29,69,86]. However, the valence band edge near the Γ-point comprises three strongly interacting bands, resulting in a complex band structure characterized by warped constant energy surfaces and nonparabolic energy dispersion, particularly evident in the lh band [29,107]. This multiband character challenges the validity of the classical isotropic and parabolic band models for hole scattering [26–28]. In contrast to conventional isotropic and parabolic single-band models, multiband models necessitate the consideration of both intraband and interband scattering processes. The role of interband scattering in hole mobility in semiconductors has been a subject of

ongoing debate. Several studies have suggested that intraband and interband scattering rates are comparable in magnitude [30,35–38]. However, this perspective is challenged by Akimoto *et al.* [28], who reported an absence of interband scattering in diamond with smaller spin-orbit splitting than Si and Ge. Despite more than five decades of research, a comprehensive understanding of the role of interband scattering in hole mobility remains elusive, emphasizing a need for further research in this field.

To assess the interband scattering in classical phenomenological approaches [30,35–38,71], we first examine the approximation using a parabolic band model to account for the nonparabolic band dispersion [109]. As previously discussed, the second top valence band transitions from the lh band (before anticrossing with such a band) to the sh band (after anticrossing). This transition makes the second top valence band (or lh band) be classically described by two parabolic sections characterized by two constant effective masses [109]: $m_{lh}^1 = m_{lh}$ and $m_{lh}^2 = m_{hh}$, as shown in Figs. 8(a) and 8(b). Consequently, in a parabolic band model, the averaged lh effective mass depends sensitively on doping concentration and temperature. Figure 8(c) shows that the second top band in a parabolic band model (characterized by an averaged lh effective mass) approaches the low-lying sh band at low temperatures and the top hh band at high temperatures. To address the temperature dependence of effective mass within the parabolic band model [110], Barber [111], Costato *et al.* [109], and Gagliani *et al.* [112] proposed a temperature-correction effective mass formula using Fermi-Dirac integrals and a simplified valence band structure based on Kane's band model [113]. Here, this approach is called the temperature-correction band (TCB) model. Using the TCB model, Linares [36–38] obtained room-temperature density-of-states effective masses of approximately 0.40 m_0 for lh and 0.55 m_0 for hh in Si. Yang *et al.* [30] reported values of 0.50 m_0, 0.41 m_0, and 0.05 m_0 for lh, and 0.53 m_0, 0.54 m_0, 0.35 m_0 for hh at
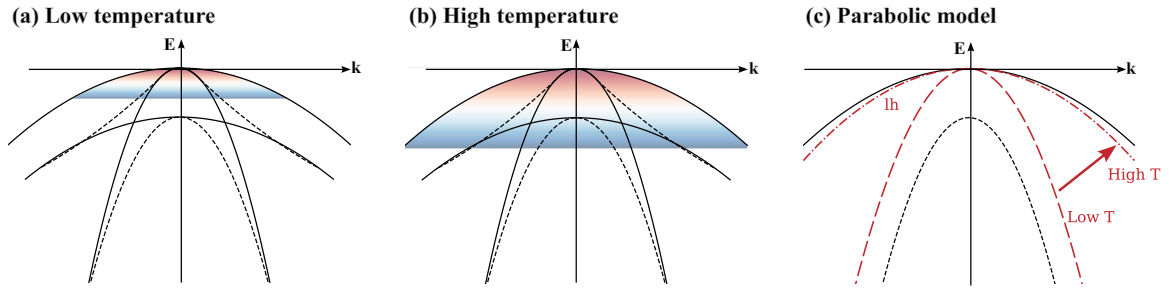
FIG. 8. Schematic nonparabolic valence band structure of diamond-structure with carrier distributions at (a) low temperatures and (b) high temperatures. Schematic parabolic valence band structure. (c) Schematic parabolic valence band structure of diamond-structure. As temperature increases, the lh band tends to approach the hh band due to the temperature-dependent increase in the effective mass of light holes, which arises from the thermal averaging of carrier energies over the nonparabolic band structure.

room temperature in the diamond, Si, and Ge, respectively. Notably, the average lh effective mass of Ge is minimally modified in the TCB model due to the large energy separation of the sh band, while in Si, it gradually approaches the hh effective mass with increasing temperature. According to the phenomenological scattering model [71], the ratio of the interband (from hh to lh) and intraband (from hh to hh) scattering rates is proportional to the ratio of the density of their final scattering states, quantified by (DOS effective mass)$^{3/2}$ of lh band for interband scattering and of hh for intraband scattering [29,30,43,71,86,114]. Consequently, at room temperature, the interband scattering rate is comparable to the intraband scattering rate in both diamond and Si, as their averaged lh effective masses are close to the hh effective mass. In contrast, the interband scattering rate is significantly smaller than the intraband scattering rate in Ge due to its much lighter averaged lh effective mass compared to the hh band.

Our first-principles calculations reveal finite interband scattering of hh states, as shown in Fig. 9. The interband scattering accounts for 15%, 15%, and 4% of the total scattering

rate at room temperature in diamond, Si, and Ge, respectively. These findings diverge from previous perspectives, which either suggested the absence of interband scattering [28] or proposed that interband scattering is comparable to intraband scattering in hole mobility [30,35–38]. The significant overestimation of interband scattering rates in diamond and Si by the temperature-correction band (TCB) model highlights its limitations in treating interband scattering accurately. Furthermore, the incorrect argument of absent interband scattering in diamond hole mobility can be attributed to the inability of classical phenomenological approaches to distinguish between interband and intraband scattering when adjusting deformation potentials to reproduce experimental hole mobility [26–28].

The **k**-dependent lh mass, affected by anticrossing, can elucidate the disparate mobility ratios between lh and hh bands in Si and Ge. In Si, the lh band mobility is only 1.6 times higher than its hh counterpart, whereas in Ge, this ratio approaches an order of magnitude. This discrepancy can be attributed to the band structure characteristics of these materials. As previously demonstrated, the lh band exhibits a light mass only near the Γ point, while maintaining a mass comparable to the hh band elsewhere due to the anticrossing between lh and split-off hole (sh) bands. In Si, the significantly smaller spin-orbit splitting Δ_{so} confines the light-mass behavior of the lh band to a narrow k-range. Consequently, the lh band mobility, described by $e\tau/m_{lh}^*(k)$, is only 1.6 times higher than the hh band mobility. In contrast, the anticrossing between lh and sh bands in Ge occurs at a much larger k-range, which does not substantially affect the lh band mobility within the investigated temperature range. As a result, the lh band mobility in Ge remains approximately an order of magnitude higher than its hh band mobility, as illustrated in Fig. 2(c).
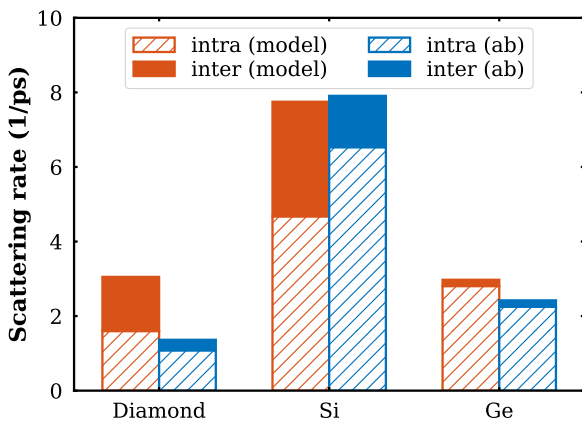

FIG. 9. Comparative analysis of heavy hole scattering rates in diamond, Si, and Ge, juxtaposing results from two distinct methodologies: (1) Light red region: Scattering rates derived from the phenomenological model [30], which incorporates empirical parameters and simplified band structures to estimate carrier scattering rates. (2) Light blue region: Scattering rates calculated using state-of-the-art *ab initio* methods in the present work. These calculations are based on density functional perturbation theory and incorporate full band structures and phonon dispersions.

IV. CONCLUSION

In this work, we investigated the anomalous hole mobility trend in Group IV semiconductors using *ab initio* Boltzmann transport formalism and presented several new findings about hole mobility that challenge long-standing assumptions: (1) The significantly larger transition matrix element in diamond gives rise to an abnormally light mass, which is a leading factor for its superior hole mobility; otherwise, diamond's hole mobility would be approximately nine times smaller than Si. (2) Diamond exhibits a unique valence band

structure, similar to the uniaxial strain-modified band structures in Si and Ge that enhance hole mobility. (3) The superior light-hole mobility in Ge explains its more efficient enhancement of hole mobility under uniaxial strain than Si, based on the heavy-hole-light-hole mixing of the top valence band.

Furthermore, our study also provides new insights into hole-phonon interactions in these materials. We first demonstrate strong coupling between holes and TA phonons, with TA scattering dominating over LA scattering in diamond and Si. The extracted dilation deformation potential in diamond from first-principles calculation hole-phonon matrices is about 3.45 eV, much smaller than previously reported values. This discrepancy underscores the limitations of classical approaches in accurately describing scattering mechanisms in diamond and highlights the importance of advanced computational methods in understanding carrier transport phenomena. Then, we find that in diamond, the strong hole-optical-phonon coupling significantly affects hole mobility by overcoming its low phonon occupation, resulting in optical scattering contributing 23% of the total scattering at room temperature and causing a sharp reduction in hole mobilities above 400 K. Finally, we reexamine the role of interband and intraband scattering mechanisms and find that the interband scattering of hh in diamond and Si only account for approximately 15% of the total hh scattering rate at room temperature. This result contradicts traditional views that either consider interband scattering negligible or highly significant.

This work provides a new understanding of the intricate mechanisms governing hole transport in diamond, Si, and Ge semiconductors. As we continue to push the boundaries of semiconductor technology, the fundamental understanding provided by this study will be crucial in guiding the development of next-generation electronic devices with improved performance and efficiency.

[1] S. M. Sze and K. K. Ng, *Physics of Semiconductor Devices*, 3rd ed. (Wiley-Interscience, Hoboken, NJ, 2007)

[2] S. L. Chuang, *Physics of Photonic Devices*, 2nd ed., Wiley series in pure and applied optics (John Wiley, Hoboken, NJ, 2009).

[3] Edited by A. Luque López and S. Hegedus, *Handbook of Photovoltaic Science and Engineering*, 2nd ed. (Wiley, Chichester, UK, 2011).

[4] G. D. Mahan and J. O. Sofo, The best thermoelectric. Proc. Natl. Acad. Sci. USA **93**, 7436 (1996).

[5] K. S. Novoselov, A. K. Geim, S. V. Morozov, D. Jiang, M. I. Katsnelson, I. V. Grigorieva, S. V. Dubonos, and A. A. Firsov, Two-dimensional gas of massless Dirac fermions in graphene, Nature (London) **438**, 197 (2005).

[6] S. Ishiwata, Y. Shiomi, J. S. Lee, M. S. Bahramy, T. Suzuki, M. Uchida, R. Arita, Y. Taguchi, and Y. Tokura, Extremely high electron mobility in a phonon-glass semimetal, Nat. Mater. **12**, 512 (2013).

[7] R. Pillarisetty, Academic and industry research progress in germanium nanodevices, Nature (London) **479**, 324 (2011).

[8] J. D. Cressler, *SiGe and Si Strained-Layer Epitaxy for Silicon Heterostructure Devices* (CRC Press, Boca Raton, FL, 2017).

[9] John D. Cressler, ed., *Silicon Heterostructure Handbook: Materials, Fabrication, Devices, Circuits and Applications of SiGe and Si Strained-Layer Epitaxy* (CRC Press, Boca Raton, FL, 2017).

[10] X.B. Deng, H. Chen, and Z.Y. Yang, Two-dimensional silicon nanomaterials for optoelectronics, J. Semicond. **44**, 041101 (2023).

[11] C. K. Maiti, S. Chattopadhyay, and L. K. Bera, *Strained-Si Heterostructure Field Effect Devices* (CRC Press, Boca Raton, FL, 2007).

[12] C. K. Maiti, Strained-Si heterostructure field effect devices: Strain-engineering in CMOS technology, in *Proceedings of the International Workshop on Physics of Semiconductor Devices* (IEEE, Mumbai, India, 2007), pp. 52–56.

[13] P. Goley and M. Hudait, Germanium based field-effect transistors: Challenges and opportunities, Materials **7**, 2301 (2014).

[14] AZO Materials, Materials Science Articles | Latest Science Articles | Scientific Development (2020), https://www.azom.com/articles.aspx.

[15] S. Adachi, *Properties of Group-IV, III–V, and II–VI Semiconductors: Adachi/Properties of Group-IV, III–V, and II–VI Semiconductors* (John Wiley & Sons, Chichester, UK, 2005).

[16] H. Lee, S. Poncé, K. Bushick, S. Hajinazar, J. Lafuente-Bartolome, J. Leveillee, C. Lian, J.-M. Lihm, F. Macheda, H. Mori, Hari Paudyal, Weng Hong Sio, Sabyasachi Tiwari, Marios Zacharias, Xiao Zhang, N. Bonini, E. Kioupakis, E. R. Margine, and F. Giustino, Electron–phonon physics from first principles using the EPW code, npj Comput. Mater. **9**, 156 (2023).

[17] W. Li, Electrical transport limited by electron-phonon coupling from Boltzmann transport equation: An *ab initio* study of Si, Al, and MoS₂, Phys. Rev. B **92**, 075405 (2015).

[18] J. Ma, A. S. Nissimagoudar, and W. Li, First-principles study of electron and hole mobilities of Si and GaAs, Phys. Rev. B **97**, 045201 (2018).

[19] T.-H. Liu, B. Song, L. Meroueh, Z.-W. Ding, Q.-C. Song, J.-W. Zhou, M.-D. Li, and G. Chen, Simultaneously high electron and hole mobilities in cubic boron-V compounds: BP, BAs, and BSb, Phys. Rev. B **98**, 081203(R) (2018).

[20] W.-H. Xiao, K. K Yang, R. D'Agosta, H.-R. Xu, G. Ouyang, G.H. Zhou, K.-Q. Chen, and L.-M. Tang, High-mobility two-dimensional MA_2N_4 (M = Mo, W; A = Si, Ge) family for transistors, Phys. Rev. B **109**, 115427 (2024).

[21] S. Poncé, E. R. Margine, and F. Giustino, Towards predictive many-body calculations of phonon-limited carrier mobilities in semiconductors, Phys. Rev. B **97**, 121201(R) (2018).

[22] J.-J. Zhou, J. Park, I-Te Lu, I. Maliyov, X. Tong, and M. Bernardi, Perturbo: A software package for *ab initio* electron-phonon interactions, charge transport and ultrafast dynamics, Comput. Phys. Commun. **264**, 107970 (2021).

[23] G. Brunin, Henrique Pereira Coutada Miranda, M. Giantomassi, M. Royo, M. Stengel, M. J. Verstraete, X. Gonze, G.-M. Rignanese, and G. Hautier, Electron-phonon beyond fröhlich: Dynamical quadrupoles in polar and covalent solids, Phys. Rev. Lett. **125**, 136601 (2020).

[24] G. Brunin, Henrique Pereira Coutada Miranda, M. Giantomassi, M. Royo, M. Stengel, M. J. Verstraete, X. Gonze, G.-M. Rignanese, and G. Hautier, Phonon-limited electron mobility in Si, GaAs, and GaP with exact treatment of dynamical quadrupoles, Phys. Rev. B **102**, 094308 (2020).

[25] M. V. Fischetti and S. E. Laux, Band structure, deformation potentials, and carrier mobility in strained Si, Ge, and SiGe alloys, J. Appl. Phys. **80**, 2234 (1996).

[26] J. Pernot, P. N. Volpe, F. Omnès, P. Muret, V. Mortet, K. Haenen, and T. Teraji, Hall hole mobility in boron-doped homoepitaxial diamond, Phys. Rev. B **81**, 205203 (2010).

[27] Y. Sasama, T. Kageura, M. Imura, K. Watanabe, T. Taniguchi, T. Uchihashi, and Y. Takahide, High-mobility p-channel wide-bandgap transistors based on hydrogen-terminated diamond/hexagonal boron nitride heterostructures, Nat. Electron. **5**, 37 (2022).

[28] I. Akimoto, Y. Handa, K. Fukai, and N. Naka, High carrier mobility in ultrapure diamond measured by time-resolved cyclotron resonance, Appl. Phys. Lett. **105**, 032102 (2014).

[29] P. Y. Yu and M. Cardona, *Fundamentals of Semiconductors: Physics and Materials Properties*, 4th ed., Graduate texts in physics (Springer, Berlin, 2010).

[30] Q.-L. Yang, H.-X. Deng, S.-H. Wei, S.-S. Li, and J.-W. Luo, Materials design principles towards high hole mobility learning from an abnormally low hole mobility of silicon, arXiv:2011.02262.

[31] D. Bimberg, R. Blachnik, M. Cardona, P. J. Dean, T. Grave, G. Harbeke, K. Hübner, U. Kaufmann, W. Kress, O. Madelung, W. von Munch, U. Rössler, J. Schneider, M. Schulz, and M. S. Skolnick, *Physics of Group IV Elements and III–V Compounds/Physik der Elemente der IV. Gruppe und der III-V Verbindungen*, edited by O. Madelung, Condensed Matter (Springer-Verlag, Berlin, 1982).

[32] NSM Archive—Physical Properties of Semiconductors, http://www.ioffe.ru/SVA/NSM/Semicond/.

[33] L. Reggiani, S. Bosi, C. Canali, F. Nava, and S. F. Kozlov, On the lattice scattering and effective mass of holes in natural diamond, Solid State Commun. **30**, 333 (1979).

[34] P. Lawaetz, Low-field mobility and galvanomagnetic properties of holes in germanium with phonon scattering, Phys. Rev. **174**, 867 (1968).

[35] F. Szmulowicz, Calculation of optical- and acoustic-phonon—Limited conductivity and Hall mobilities for *p*-type silicon and germanium, Phys. Rev. B **28**, 5943 (1983).

[36] L. C. Linares and S. S. Li, An improved model for analyzing hole mobility and resistivity in p-type silicon doped with boron, gallium, and indium, J. Electrochem. Soc. **128**, 601 (1981).

[37] J. F. Lin, S. S. Li, L. C. Linares, and K. W. Teng, Theoretical analysis of Hall factor and Hall mobility in p-type silicon, Solid-State Electron. **24**, 827 (1981).

[38] L. C. Linares, The Mobility, Resistivity and carrier density in P-type silicon doped with boron, gallium and indium, Ph.D. thesis, University of Florida, Gainesville, FL, 1979.

[39] M. Chu, Y. K. Sun, U. Aghoram, and S. E. Thompson, Strain: A solution for higher carrier mobility in nanoscale MOSFETs, Annu. Rev. Mater. Res. **39**, 203 (2009).

[40] N. Mohta and S.E. Thompson, Mobility enhancement, IEEE Circ. Dev. Mag. **21**, 18 (2005).

[41] Q.-L. Yang, W. Li, Z. Wang, F.-L. Ning, and J.-W. Luo, Uncovering the important role of transverse acoustic phonons in the carrier-phonon scattering in silicon, Phys. Rev. B **109**, 125203 (2024).

[42] S. Poncé, W. B. Li, S. Reichardt, and F. Giustino, First-principles calculations of charge carrier mobility and conductivity in bulk semiconductors and two-dimensional materials, Rep. Prog. Phys. **83**, 036501 (2020).

[43] P. Giannozzi, O. Andreussi, T. Brumme, O. Bunau, M. Buongiorno Nardelli, M. Calandra, R. Car, C. Cavazzoni, D. Ceresoli, M. Cococcioni, N. Colonna, I. Carnimeo, A. D. Corso *et al.*, Advanced capabilities for materials modelling with quantum ESPRESSO, J. Phys.: Condens. Matter **29**, 465901 (2017).

[44] S. Poncé, E. R. Margine, C. Verdi, and F. Giustino, Epw: Electron-phonon coupling, transport and superconducting properties using maximally localized Wannier functions, Comput. Phys. Commun. **209**, 116 (2016).

[45] J. Noffsinger, F. Giustino, B. D. Malone, C. H. Park, S. G. Louie, and M. L. Cohen, EPW: A program for calculating the electron-phonon coupling using maximally localized Wannier functions, Comput. Phys. Commun. **181**, 2140 (2010).

[46] S. Baroni, S. de Gironcoli, A. Dal Corso, and P. Giannozzi, Phonons and related crystal properties from density-functional perturbation theory, Rev. Mod. Phys. **73**, 515 (2001).

[47] A. A. Mostofi, J. R. Yates, G. Pizzi, Y.-S. Lee, I. Souza, D. Vanderbilt, and N. Marzari, An updated version of Wannier90: A tool for obtaining maximally localised Wannier functions, Comput. Phys. Commun. **185**, 2309 (2014).

[48] F. Giustino, M. L. Cohen, and S. G. Louie, Electron-phonon interaction using Wannier functions, Phys. Rev. B **76**, 165108 (2007).

[49] M. Gabrysch, S. Majdi, D. J. Twitchen, and J. Isberg, Electron and hole drift velocity in chemical vapor deposition diamond, J. Appl. Phys. **109**, 063719 (2011).

[50] F. J. Morin and J. P. Maita, Electrical properties of silicon containing arsenic and boron, Phys. Rev. **96**, 28 (1954).

[51] R. A. Logan and A. J. Peters, Impurity effects upon mobility in silicon, J. Appl. Phys. **31**, 122 (1960).

[52] G. W. Ludwig and R. L. Watters, Drift and conductivity mobility in silicon, Phys. Rev. **101**, 1699 (1956).

[53] C. Jacoboni, C. Canali, G. Ottaviani, and A. Alberigi Quaranta, A review of some charge transport properties of silicon, Solid-State Electron. **20**, 77 (1977).

[54] G. Ottaviani, C. Canali, F. Nava, and J. W. Mayer, Hole drift velocity in high-purity Ge between 8 and 220 °K, J. Appl. Phys. **44**, 2917 (1973).

[55] F. J. Morin, Lattice-scattering mobility in germanium, Phys. Rev. **93**, 62 (1954).

[56] E. G. S. Paige, The drift mobility of electrons and holes in germanium at low temperatures, J. Phys. Chem. Solids **16**, 207 (1960).

[57] A. A. El-Difrawi, Drift mobility of holes in n-type germanium bombarded by fast neutrons, J. Appl. Phys. **47**, 272 (1976).

[58] D. M. Brown and R. Bray, Analysis of lattice and ionized impurity scattering in *p*-type germanium, Phys. Rev. **127**, 1593 (1962).

[59] G.Y. Sun, Strain effects on hole mobility of silicon and germanium p-type metal-oxide-semiconductor field-effect-transistors, Ph.D. thesis, University of Florida, Gainesville, FL, 2007.

[60] Th. Vogelsang and K. R. Hofmann, Electron transport in strained Si layers on Si$_{1-x}$Ge$_x$ substrates, Appl. Phys. Lett. **63**, 186 (1993).

[61] M. V. Fischetti, Z. Ren, P. M. Solomon, M. Yang, and K. Rim, Six-band k.p calculation of the hole mobility in silicon inversion layers: Dependence on surface orientation, strain, and silicon thickness, J. Appl. Phys. **94**, 1079 (2003).

[62] Y. Zhang, M. V. Fischetti, B. Sorée, and T. O'Regan, Theory of hole mobility in strained Ge and III–V p-channel inversion layers with high-κ insulators, J. Appl. Phys. **108**, 123713 (2010).

[63] J. A. Alamo, Nanometre-scale electronics with III–V compound semiconductors, Nature (London) **479**, 317 (2011).

[64] K. J. Kuhn, A. Murthy, R. Kotlyar, and M. Kuhn, Past, present and future: SiGe and CMOS transistor scaling, ECS Trans. **33**, 3 (2010).

[65] L. Gomez, C. Ni Chléirigh, P. Hashemi, and J. L. Hoyt, Enhanced hole mobility in high ge content asymmetrically strained-SiGe p-MOSFETS, IEEE Electron Device Lett. **31**, 782 (2010).

[66] H. Hasegawa, Theory of cyclotron resonance in strained silicon crystals, Phys. Rev. **129**, 1029 (1963).

[67] J. C. Hensel and G. Feher, Cyclotron resonance experiments in uniaxially stressed silicon: Valence band inverse mass parameters and deformation potentials, Phys. Rev. **129**, 1041 (1963).

[68] K. J. Kuhn, Considerations for ultimate CMOS scaling, IEEE Trans. Electron Devices **59**, 1813 (2012).

[69] M. Lundstrom, *Fundamentals of Carrier Transport*, 2nd ed. (Cambridge University Press, Cambridge, UK/New York, NY, 2000).

[70] J. D. Wiley, Mobility of holes in III-V compounds, in *Semiconductors and Semimetals*, edited by R. K. Willardson and Albert C. Beer Vol. 10 (Elsevier, Amsterdam, 1975), Chap. 2, pp. 91–174.

[71] V. F. Gantmakher and I. B. Levinson, *Carrier Scattering in Metals and Semiconductors*, Modern Problems in Condensed Matter Sciences No. 19 (North-Holland, Amsterdam/New York, NY, 1987).

[72] F. L. Madarasz and F. Szmulowicz, Transition rates for acoustic-phonon-hole scattering in *p*-type silicon with nonparabolic bands, Phys. Rev. B **24**, 4611 (1981).

[73] M. Tiersten, Acoustic-mode scattering of holes, IBM J. Res. Dev. **5**, 122 (1961).

[74] M. Tiersten, Acoustic-mode scattering mobility of holes in diamond type semiconductors, J. Phys. Chem. Solids **25**, 1151 (1964).

[75] G. L. Bir and G. E. Pikus, *Symmetry and Strain-induced Effects in Semiconductors* (Wiley, New York, NY, 1974).

[76] G. S. Cargill, J. Angilello, and K. L. Kavanagh, Lattice compression from conduction electrons in heavily doped Si:As, Phys. Rev. Lett. **61**, 1748 (1988).

[77] D. D. Nolte, W. Walukiewicz, and E. E. Haller, Band-edge hydrostatic deformation potentials in III–V semiconductors, Phys. Rev. Lett. **59**, 501 (1987).

[78] M. Cardona and N. E. Christensen, Acoustic deformation potentials and heterostructure band offsets in semiconductors, Phys. Rev. B **35**, 6182 (1987).

[79] C. G. Van de Walle, Band lineups and deformation potentials in the model-solid theory, Phys. Rev. B **39**, 1871 (1989).

[80] S.-H. Wei and A. Zunger, Predicted band-gap pressure coefficients of all diamond and zinc-blende semiconductors: Chemical trends, Phys. Rev. B **60**, 5404 (1999).

[81] M. H. Grimsditch, E. Anastassakis, and M. Cardona, Piezobirefringence in diamond, Phys. Rev. B **19**, 3240 (1979).

[82] A. Blacha, H. Presting, and M. Cardona, Deformation potentials of $k = 0$ states of tetrahedral semiconductors, Phys. Status Solidi B **126**, 11 (1984).

[83] J.D. Wiley, Valence-band deformation potentials for the III–V compounds, Solid State Commun. **8**, 1865 (1970).

[84] M. Cardona and N. E. Christensen, Deformation potentials of the direct gap of diamond, Solid State Commun. **58**, 421 (1986).

[85] Y.-H. Li, X. G. Gong, and S.-H. Wei, *Ab initio* all-electron calculation of absolute volume deformation potentials of IV–IV, III–V, and II–VI semiconductors: The chemical trends, Phys. Rev. B **73**, 245206 (2006).

[86] C. Hamaguchi, *Basic Semiconductor Physics*, 3rd ed., Graduate texts in physics (Springer, Cham, 2017).

[87] M. Abramowitz and I. A. Stegun, *Handbook of Mathematical Functions: With Formulas, Graphs and Mathematical Tables*, unabridged, unaltered and corr. republ. of the 1964 ed., Dover Books on Advanced Mathematics (Dover, New York, NY, 1972).

[88] H. Löfås, A. Grigoriev, J. Isberg, and R. Ahuja, Effective masses and electronic structure of diamond including electron correlation effects in first principles calculations using the GW-approximation, AIP Adv. **1**, 032139 (2011).

[89] M. Willatzen, M. Cardona, and N. E. Christensen, Linear muffin-tin-orbital and $k \cdot p$ calculations of effective masses and band structure of semiconducting diamond, Phys. Rev. B **50**, 18054 (1994).

[90] M. T. Edmonds, A. Tadich, M. Wanke, K. M. O'Donnell, Y. Smets, K. J. Rietwyk, J. D. Riley, C. I. Pakes, and L. Ley, Valence-band structure and critical point energies of diamond along [100], Phys. Rev. B **87**, 085123 (2013).

[91] N. Naka, K. Fukai, Y. Handa, and I. Akimoto, Direct measurement via cyclotron resonance of the carrier effective masses in pristine diamond, Phys. Rev. B **88**, 035205 (2013).

[92] V. K. Bashenov, A. G. Gontar, and A. G. Petukhov, Excited states of a shallow acceptor in semiconducting diamond from photoconductivity spectra, Phys. Status Solidi B **108**, K139 (1981).

[93] J. Kono, S. Takeyama, T. Takamasu, N. Miura, N. Fujimori, Y. Nishibayashi, T. Nakajima, and K. Tsuji, High-field cyclotron resonance and valence-band structure in semiconducting diamond, Phys. Rev. B **48**, 10917 (1993).

[94] C. J. Rauch, Millimeter cyclotron resonance experiments in diamond, Phys. Rev. Lett. **7**, 83 (1961).

[95] L. E. Ramos, L. K. Teles, L. M. R. Scolfaro, J. L. P. Castineira, A. L. Rosa, and J. R. Leite, Structural, electronic, and effective-mass properties of silicon and zinc-blende group-III

nitride semiconductor compounds, Phys. Rev. B **63**, 165210 (2001).

[96] J. Kim and M. V. Fischetti, Electronic band structure calculations for biaxially strained Si, Ge, and III–V semiconductors, J. Appl. Phys. **108**, 013710 (2010).

[97] M. V. Fischetti and J. M. Higman, Theory and calculation of the deformation potential electron-phonon scattering rates in semiconductors, in *Monte Carlo Device Simulation: Full Band and Beyond*, edited by Karl Hess (Springer US, Boston, MA, 1991), pp. 123–160.

[98] D. V. Savchenko, E. N. Kalabukhova, B. D. Shanina, N. T. Bagraev, L. E. Klyachkin, A. M. Malyarenko, and V. S. Khromov, Electron and hole effective masses in heavily boron doped silicon nanostructures determined using cyclotron resonance experiments, Semicond. Phys. Quant. Electr. Optoelectr. **21**, 249 (2018).

[99] R. N. Dexter and B. Lax, Effective masses of holes in silicon, Phys. Rev. **96**, 223 (1954).

[100] R. N. Dexter, H. J. Zeiger, and Benjamin Lax, Cyclotron resonance experiments in silicon and germanium, Phys. Rev. **104**, 637 (1956).

[101] K. Lu Low, Y. Yang, G. Q. Han, W. J. Fan, and Y.-C. Yeo, Electronic band structure and effective mass parameters of $Ge_{1-x}Sn_x$ alloys, J. Appl. Phys. **112**, 103715 (2012).

[102] L. C. Lew Yan Voon and M. Willatzen, *The k.p Method: Electronic Properties of Semiconductors* (Springer, Dordrecht/New York, 2009).

[103] R. Winkler, *Spin-Orbit Coupling Effects in Two-Dimensional Electron and Hole Systems*, Springer Tracts in Modern Physics (Springer, Berlin, 2003).

[104] P. Lawaetz, Valence-band parameters in cubic semiconductors, Phys. Rev. B **4**, 3460 (1971).

[105] J. A. Van Vechten, Quantum dielectric theory of electronegativity in covalent systems. I. Electronic dielectric constant, Phys. Rev. **182**, 891 (1969).

[106] J. C. Phillips, *The Fundamental Optical Spectra of Solids* (Academic Press, San Diego, CA, 1966), pp. 55–164.

[107] W. A. Harrison, *Electronic Structure and the Properties of Solids: The Physics of the Chemical Bond* (Dover Publications, New York, NY, 1989).

[108] W. A. Harrison, *Elementary Electronic Structure* (World Scientific, Singapore, 1999).

[109] M. Costato and L. Reggiani, Temperature-dependence of the combined effective mass of holes in silicon, Lett. Nuovo Cimento **3**, 239 (1970).

[110] D. M. Riffe, Temperature dependence of silicon carrier effective masses with application to femtosecond reflectivity measurements, J. Opt. Soc. Am. B **19**, 1092 (2002).

[111] H.D. Barber, Effective mass and intrinsic concentration in silicon, Solid-State Electron. **10**, 1039 (1967).

[112] G. Gagliani and L. Reggiani, Nonparabolicity and intrinsic carrier concentration in Si and Ge, Il Nuovo Cimento B **30**, 207 (1975).

[113] E.O. Kane, Energy band structure in p-type germanium and silicon, J. Phys. Chem. Solids **1**, 82 (1956).

[114] M. Costato and L. Reggiani, Scattering probabilities for holes. I. Deformation potential and ionized impurity scattering mechanisms, Phys. Status Solidi B **58**, 471 (1973).